HIRA-dependent boundaries between H3 variants shape early replication in mammals

Alberto Gatto, Audrey Forest, Jean-Pierre Quivy, Geneviève Almouzni

Version of Record: https://www.sciencedirect.com/science/article/pii/S1097276522002556
Manuscript_ffdad974f857f4c912496d660c7d0434

HIRA-dependent boundaries between H3 variants shape early replication in mammals

Alberto Gatto [1], Audrey Forest [1], Jean-Pierre Quivy [1, 2], Geneviève Almouzni [1, 2, 3]

[1] Institut Curie, PSL Research University, CNRS, Sorbonne Université, Nuclear Dynamics Unit, Equipe Labellisée Ligue contre le Cancer, 26 rue d'Ulm, 75005 Paris, France

[2] corresponding authors

[3] lead contact

Correspondence: genevieve.almouzni@curie.fr; jean-pierre.quivy@curie.fr

Summary

The lack of consensus DNA sequence defining replication origins in mammals has led to consider chromatin as a means to specify these regions. However, to date, there is no mechanistic understanding for how this could be achieved and maintained given that nucleosome disruption occurs with each fork passage and with transcription. Here, by mapping genome-wide the *de novo* deposition of the histone variants H3.1 and H3.3 in human cells during S phase, we identify how their dual deposition mode ensures a stable marking with H3.3 flanked on both sides by H3.1. These H3.1/H3.3 boundaries correspond to the initiation zones of early origins. Loss of the H3.3 chaperone HIRA leads to the concomitant disruption of H3.1/H3.3 boundaries and initiation zones. We propose that the HIRA-dependent deposition of H3.3 preserves H3.1/H3.3 boundaries by protecting them from H3.1 invasion linked to fork progression, contributing to a chromatin-based definition of early replication zones.

Keywords

histone H3 variants; DNA replication; histone chaperones; genome-wide chromatin mapping; mammalian replication origins

Introduction

Genome replication in mammals follows a defined spatiotemporal program established during early development (DePamphilis et al., 2016). This program adapts to changes in gene expression during differentiation (Hiratani et al., 2008; Hiratani et al., 2010; Rivera-Mulia et al., 2015; Rausch et al., 2020) and is severely impacted by oncogene activation in cancer cells (Macheret and Halazonetis, 2018). These changes highlight the fact that DNA sequences cannot suffice to define a replication program. Indeed, in metazoans, chromatin features have been further invoked in this definition (Fragkos et al., 2015; Marchal et al., 2019). DNA synthesis usually starts in active chromatin, where distinct marks decorate transcribed regions and regulatory elements according to the expression profiles of each cell type (Romanoski et al., 2015). However, these regions undergo dynamic changes throughout the cell cycle (Deal et al., 2010), challenging the stability of a marking system that relies solely on post-translational modifications (PTMs). Indeed, histones, the building blocks of chromatin, are continuously disrupted by transcription, replication and repair (Probst et al., 2009; Stewart-Morgan et al., 2020). Thus, what defines initiation zones remains elusive, and how to maintain a given chromatin state in the face of all these challenges is a question which has proven particularly critical for active marks (Ray-Gallet and Almouzni, 2010; Reinberg and Vales, 2018). If information carried by histones is key for replication initiation, how to preserve it when challenged during S phase? Indeed, the passage of the replication fork entails the disruption of parental nucleosomes and doubles the amount of DNA. Thus, to restore nucleosome density on both DNA copies, both recycling of parental histones and a complement of newly synthesized histones are necessary (Almouzni and Cedar, 2016; Stewart-Morgan et al., 2020). Since newly deposited histones lack parental marks, their incorporation is a challenge for preserving the chromatin states that direct the replication program.

When considering histone-based information, one has to consider not only the range of post-translational modifications that decorate them (Martire and Banaszynski, 2020) but also the diversity of histone variants (Szenker et al., 2014; Buschbeck and Hake 2017). We recently found that, in asynchronous cells, the distribution of histone H3 variants shows a striking correlation with replication timing (Clément et al., 2018). H3.3 marks early-replicating sites in active chromatin, while H3.1 is broadly enriched at inactive, late-replicating regions (Clément et al., 2018). These observations led us to consider whether H3.1 and H3.3 deposition could actually be critical to preserve chromatin organization in early-replicating regions. While their distinct deposition pathways theoretically compensate for histone loss during both replication and transcription (Ray-Gallet and Almouzni, 2021), the dominance of one pathway during S phase could affect the propagation of existing marks on replicating chromatin. Indeed, H3.1 deposition occurs in a DNA synthesis-coupled (DSC) manner (Tagami et al., 2004) thanks to the CAF-1 complex, recruited by PCNA at the replication fork (Shibahara and Stillman, 1999). H3.3 is instead deposited throughout the cell cycle in a DNA synthesis-independent (DSI) manner by the HIRA complex (Tagami et al., 2004; Ray-Gallet et al. 2011; Torné et al., 2020) and accumulates at high-turnover sites (Deal et al., 2010) in active chromatin (Goldberg et al., 2010). Intriguingly, H3.3 is also enriched at non-transcribed regions, and its correlation with replication timing proved independent of transcriptional activity (Clément et al., 2018). This suggested a link

between replication and H3.3 which may be independent of its deposition with transcription. While new H3.1 deposition during S phase has been considered, new H3.3 deposition is less defined during this time window. We thus wanted to explore how the *de novo* deposition of two distinct variants using distinct pathways could contribute to a marking system that preserves initiation patterns on the replicating genome.

Here, we develop an assay to map newly deposited H3.1 and H3.3 during S phase, at a genome-wide scale. We find that both variants are deposited on replicating chromatin. While new H3.1 tracks fork progression during S phase, new H3.3 targets the same locations where preexisting H3.3 accumulates outside of S phase. This dual deposition produces a genome-wide footprint of early fork progression, where H3.1/H3.3 boundaries mark the initiation zones (IZ) of early-firing origins. Remarkably, the H3.3 chaperone HIRA is required not only to preserve these boundaries, but also to define the location of early replication zones. We propose that, when histones are displaced during fork passage, *de novo* deposition pathways - by restricting the locations where parental histones can be inherited - preserve preexisting H3.1/H3.3 boundaries that are critical for replication initiation. We discuss the implications for epigenome maintenance and reprogramming during normal or pathological cell fate transitions.

Results

Monitoring histone deposition during S phase by cell synchronization coupled to SNAP-tag capture

To investigate *de novo* H3.1 and H3.3 deposition during S phase at genome-wide resolution, we developed a SNAP capture and sequencing assay (SNAP-Seq). Using the SNAP-tag to discriminate newly synthesized histones from preexisting ones, we devised a "quench-chase-capture" strategy (Figure 1A). We synchronized HeLa cells stably expressing H3.1- or H3.3-SNAP in G1/S using a double-thymidine block. After MNase digestion, by selectively isolating new H3.1- and H3.3-containing nucleosomes and sequencing the corresponding DNA, we profiled their distribution after release into S phase. As a prerequisite, we first assessed the kinetics of EdU incorporation over a 10h time course in synchronized H3.1-SNAP cells (Figure S1A and S1B). This allowed us to select optimal time windows (from 2.0h to 5.0h) with comparable incorporation across cells, and reproducible in H3.3-SNAP cells (Figure S1B). Prior to release, we did not detect EdU incorporation (EdU, 0.0h) in both H3.1- and H3.3-SNAP cells. After 2.0h, ~90% cells showed typical of early S phase patterns, with diffuse EdU staining throughout the nucleus. At 5.0h, mid S phase patterns became prevalent with ~85% cells presenting EdU enrichment at the nuclear periphery and around nucleoli. We thus considered these 2.0h and 5.0h time points as representative of replication patterns from early to mid S phase. Importantly, we found homogeneous patterns across cells in both H3.1- and H3.3-SNAP cell lines (Figure S1C and S1D). In parallel, we assessed the *de novo* deposition of H3.1 or H3.3 by quench-chase-pulse labeling (Figure 1B, TMR). In line with a deposition mode coupled to DNA synthesis, new H3.1 at 0.0h was undetectable and, after release into S phase, followed patterns observed for EdU: a diffuse nuclear staining in early S (2.0h) and perinuclear or nucleolar enrichment in mid S (5.0h). In contrast, we detected new H3.3 both before (G1/S, 0.0h) and after release into S phase (2.0h and 5.0h), with a broad nuclear localization in line with its deposition mode uncoupled from DNA synthesis, irrespective of the S phase progression (Figure 1B). Based on these data, we concluded that our experimental set-up allows to monitor the distinct deposition of H3.1 and H3.3 in both cell lines in a consistent and reproducible manner from early (2.0h) to mid (5.0h) S phase. We thus selected these two time points to probe H3.1 and H3.3 genome-wide dynamics during DNA replication.

During S phase, new H3.1 deposition follows the replication fork while new H3.3 replenishes sites previously marked with H3.3, independently of S phase progression

With our SNAP-Seq method, we compared the *de novo* deposition of H3.1 and H3.3 in synchronized cells from early (2.0 h) to mid S (5.0 h) phase with their initial distribution in G1/S (0.0 h) (Figure 2A). We assessed replication timing across the genome using available Repli-Seq data (Dellino et al., 2013, Figure 2B). Similar to asynchronous cells (Clément et al., 2018), in G1/S, H3.1 and H3.3 showed a reciprocal genome-wide distribution: H3.3 marked early-replicating sites while H3.1 was broadly enriched at late-replicating regions. However, 2.0h after release in S phase, deposition of new H3.1 occurred first at sites of H3.3 enrichment, in a complementary manner to its G1/S distribution. This deposition changed gradually as cells progressed in S phase (Figure 2C and Figure S2A). Consistent with the model of DSC deposition by CAF-1 (Taddei et al., 1999), the deposition of new H3.1 followed the timing of DNA synthesis as measured by

Repli-Seq (cf. Figure 2B and 2C). In G1/S, H3.1 enrichment marked mostly late-replicating chromatin but, 2.0h after entry into S phase, early-replicating regions showed a strong enrichment while late-replicating ones became depleted. Then, after 5.0h, new H3.1 extended further from the early deposition sites, spreading bidirectionally to expand into regions that replicate in mid S phase (cf. BrdU incorporation from S_1 to S_3 in Figure 2B). We strengthened this observation genome-wide by evaluating the mean H3.1 and H3.3 enrichment according to replication timing (S_1 to S_6, Figure 2E). This confirmed that H3.1 enrichment peaked at early-replicating regions 2.0h after release and at mid-replicating regions at 5.0h (top panels). In contrast to H3.1, new H3.3 deposition was invariant over the same time course (Figure 2D and Figure S2B). H3.3 deposition was restricted to early-replicating sites, where new H3.3 was systematically deposited independently of S phase progression (bottom panels). Throughout the genome, H3.3 constantly replenishes preexisting sites, and its deposition is directly proportional to its G1/S enrichment (Figure S2B). We concluded that *de novo* deposition of both H3.1 and H3.3 occurred during DNA replication, but with distinct patterns. New H3.1 spread over the genome with fork progression during the course of S phase, while H3.3 deposition targeted pre-marked sites irrespective of fork progression. First, these results validated directly the model of H3.1 deposition coupled to fork progression based on imaging and immunoprecipitation studies. Second, they revealed a unique feature of H3.3 deposition on replicating chromatin that preserved its initial distribution: a means to dynamically maintain a precise marking of the genome with histone variants.

H3.1 deposition starts at the boundaries of preexisting sites marked by H3.3

In early S phase, the deposition of new H3.1 started at the same sites where H3.3 was stably enriched. To deepen our analysis of their distinct deposition around these sites, we applied a 3-state Hidden Markov Model (HMM) to detect regions specifically associated to H3.3. Having identified all the locations where, prior to S phase, H3.3 is the predominant variant (Figure S3A, G1/S), we filtered these locations based on enrichment relative to input and detected a total of 2926 H3.3 sites at 10% FDR (Table S2). These sites marked regions of ~100 kb spanning multiple genes (Figure S3B), clustered in larger domains of broad H3.3 enrichment (Figure S3C). However, each site was delimited by narrow boundaries where H3.1 was the prevalent variant (Figure S3C). During S phase, new H3.3 deposition precisely occurred in the areas within these boundaries, thereby maintaining the same distribution observed in G1/S (Figure 3A). In contrast, before replication, H3.1 showed a mutually exclusive profile, depleted from the H3.3-rich core but strongly enriched at the two boundaries (Figure 3B, G1/S). These boundaries coincided with the early sites of H3.1 deposition upon release into S phase. Indeed, 2.0h after release, new H3.1 strongly accumulated at the flanks of all H3.3 sites, and then spread bidirectionally with S phase progression after 5.0h (Figure 3B, 2.0h and 5.0h). Importantly, the targeted replacement by new H3.3 provided a means to restore the profile observed in G1/S, with H3.1 depletion at the H3.3-rich core inside the boundaries. Next, we compared H3.1 and H3.3 deposition to replication timing. Using Repli-Seq data (Dellino et al., 2013), we found that sites of H3.3 enrichment/deposition correlated with a peak of DNA synthesis in early S (Figure 3C). Replication started at the borders of each site, rapidly converging at the H3.3 core and then moving outwards in mid/late S phase.

This DNA synthesis pattern mirrored H3.1 deposition (cf. Figure 3B). Therefore, during S phase, the dynamics of deposition of the two variants ensure the maintenance of boundaries between them.

H3.3 deposition marks early replication zones even in the absence of active transcription

To better characterize chromatin organization at H3.1/H3.3 boundaries, we first examined the distribution of "active" and "repressive" marks around H3.3 sites (Figure S4). We found that H3.1/H3.3 boundaries generally occur at the transition between areas of active turnover (enriched in POL2RA, H3K36me3 and H3K79me2, and depleted in H3K27me3) and regulatory sites at the flanks (enriched in H3 methylated on K4, particularly H3K4me3, and H3K27ac) surrounded by H3K27me3 repressive marks (Figure S4A). The enrichment in active marks was consistent with the strong correlation between H3.3 enrichment and active transcription at the core region within the boundaries (Figure S4B, nascent RNA-Seq data from Liang et al., 2015). We then asked if transcription was a strict requirement for *de novo* H3.3 deposition. For this, we compared H3.3 patterns to replication timing and transcription before (total, G1/S) and after release into S phase (new, 2.0h). Remarkably, we found a systematic H3.3 enrichment even at low to undetectable levels of nascent transcription (Figure 4), which marked early replication zones in non-transcribed regions (Figure 4A, red arrow). We further compared early deposition patterns for both variants between the sites at the lowest expression percentile (Figure 4B bottom 5%, RNA^-) and all other H3.3 sites (Figure 4B, top 95%, RNA^+). Despite showing little to no evidence of nascent transcription, RNA^- sites exhibited the same H3.1/H3.3 distribution of actively transcribed ones (cf. top 95%, RNA^+), with H3.1 flanking H3.3 peaks in G1/S cells (left panels). Remarkably, both transcribed (RNA^+) and non-transcribed (RNA^-) sites showed analogous deposition patterns after release into S phase (right panels). This indicates that this marking is not merely reflecting active transcription. Thus, H3.3 stably marks early replication zones where *de novo* H3.1 deposition starts at the boundaries in early S, even in the absence of transcription.

H3.1/H3.3 boundaries demarcate the initiation zones of early-firing origins

Based on H3.1 and H3.3 deposition, we hypothesized that H3.1/H3.3 boundaries could preserve a stable footprint of replication initiation events tracking fork passage in early S phase. We thus checked the distribution of both variants in G1/S at all IZ detectable from OK-Seq data in asynchronous cells (Petryk et al., 2016, Figure 5A). Based on H3.3 enrichment around each IZ, we could discriminate IZ located in early-replicating regions, H3.3-rich ($H3.3^+$) from IZ in late-replicating regions, H3.3-poor ($H3.3^-$). $H3.3^+$ IZ, strongly enriched in nascent DNA from early S phase fractions, contrasted with $H3.3^-$ IZ, that mostly replicated in late S phase (Figure S5A, Repli-Seq data from Dellino et al., 2013). In early-replicating regions, $H3.3^+$ IZ co-localized with the H3.1-rich borders between adjacent H3.3 sites (Figure S3C) and thus overlapped the peak of H3.1 at their boundary (Figure 5A, top panels). Of note, rather than the center of each H3.3 site (Figure 3 and 4B), we visualized H3.1 and H3.3 signals from a different viewpoint here, centered at the IZ itself. $H3.3^+$ IZ localize at the flanks of H3.3 sites, overlapping the narrow H3.1 boundary that separates consecutive peaks. Consequently, this complementary viewpoint lead to reverse H3 patterns: H3.1 peaks at the center (i.e. the boundary, where early IZ are located) and H3.3 at the flanks (i.e. two adjacent sites separated by the boundary). Instead, IZ in late-replicating regions, broadly enriched in H3.1, did not co-

localize at boundaries and only showed a faint H3.3 signal (H3.3$^-$ IZ, bottom panels). Using EdU-HU-Seq data (Macheret and Halazonetis, 2018) we compared early origin firing between H3.3$^+$ and H3.3$^-$ IZ. Remarkably, we found that only origins at H3.3$^+$ IZ showed evidence of early firing (EdU HU$^+$, Figure 5A). Thus, co-localization with H3.1/H3.3 boundaries could discriminate the subset of IZ where origins fire in early S. Given the recent involvement of the H2A replacement variant H2A.Z in the activation of early origins (Long et al., 2020), we also examined its distribution across H3.3 sites (Figure S5B). Similar to H3.1, and in line with the co-localization of early IZ, we found an enrichment of H2A.Z at the two boundaries and a strong depletion within the H3.3-rich core. We then used available SNS-Seq, OK-Seq and EdU-HU-Seq data (Besnard et al., 2012; Petryk et al., 2016; Macheret and Halazonetis, 2018) to further characterize replication initiation patterns at H3.1/H3.3 boundaries (Figure 5B and Figure S5). We compared replication fork directionality (RFD), early origin firing (EdU HU$^+$) and nascent DNA strand enrichment (SNS) across all H3.3 sites that we previously detected. In line with the co-localization of early IZ at their boundaries (Figure 5A, H3.3$^+$ IZ), two well-defined IZ delimited these regions. From each boundary, forks diverged in opposite directions and converged midway in the H3.3-rich core (RFD in Figure 5B and Figure S5C). We further identified early firing at these boundaries, based on EdU-HU-Seq data (EdU HU$^+$ in Figure 5A and Figure S5D) and enrichment in nascent DNA strands (SNS, Figure S5E). Taken together, our results raised the interesting possibility that the distinct deposition of H3.1 and H3.3 could mark the IZ of early-firing origins by coupling replication initiation with the re-establishment of H3.1/H3.3 boundaries (Figure 5C). We thus asked if disrupting existing boundaries could impact early replication.

HIRA loss disrupts H3.3 targeting at preexisting sites and alters S phase progression without affecting fork speed

The re-establishment of H3.1/H3.3 boundaries relies on H3.3 targeting independent of S phase progression, to replace H3.1 within the boundaries of early replication zones. To check if these boundaries are critical for replication, we thus aimed to elucidate S phase dynamics after disrupting H3.3 deposition. Since the HIRA complex is involved in H3.3 deposition not only at active sites (Goldberg et al., 2010), but also more broadly (Ray-Gallet et al., 2011), we used stable HIRA knockout cell lines (HIRA^{KO}) expressing H3.1- or H3.3-SNAP, and corresponding control cells (HIRA^{WT}) from Ray-Gallet et al., 2018. To examine the targeting of H3.3 during DNA replication, we probed *de novo* H3.3 deposition in synchronized HIRA^{WT} and HIRA^{KO} cells, 2.0h after release into S phase. In the absence of HIRA, deposition patterns changed drastically and H3.3 could no longer target preexisting sites (Figure 6A). Rather than being restricted within defined boundaries, H3.3 accumulated at the boundaries themselves, resembling the early incorporation of new H3.1 (cf. Figure 3B). We thus concluded that HIRA was necessary to enable a proper targeting of H3.3 to preexisting sites in early S phase. Next, we investigated whether the loss of HIRA had an impact on S phase itself. By EdU pulse labeling in synchronized cells, we found that HIRA deletion significantly reduced the fraction of EdU$^+$ cells 2.0h after release into S phase and, to a lesser extent, at 5.0h (Figure 6B). Examination of EdU staining patterns further revealed that the proportion of early, mid and late S phase patterns remained similar at 2.0h for both HIRA^{WT} and HIRA^{KO} cells. However, 5.0h after release, a high proportion of

HIRA^{KO} cells still showed early S patterns, and the percentage of mid S phase cells decreased compared to HIRA^{WT} (Figure 6C). Importantly, both H3.1-SNAP and H3.3-SNAP cell lines showed a similar behavior after HIRA deletion. These data indicate that HIRA loss leads to delays in early S phase progression due either to initiation defects, slower replication fork speed, or both. We hence assessed the speed of replication fork movement in HIRA^{WT} and HIRA^{KO} cells by DNA combing (Figure 6D) and found comparable average fork speeds in the two conditions, both in asynchronous cells as well as in early-replicating cells (Figure 6E). Taken together, these results indicated the necessity of HIRA to direct H3.3 within the boundaries that mark IZ. Furthermore, since HIRA loss altered S phase progression without affecting fork speed, an impaired H3.3 targeting could directly affect replication initiation in early S.

Local H3.3 targeting by HIRA is critical to preserve early replication zones

Our data showed that HIRA-mediated H3.3 deposition occurred within boundaries that marked IZ, and that HIRA loss may affect initiation itself. To further characterize the impact of HIRA deletion at a genome-wide scale, we probed the effect on early replication patterns in relation to H3.1 and H3.3. To this aim, we characterized the G1/S distribution of H3.1 and H3.3 in HIRA^{WT} and HIRA^{KO} cells, and profiled EdU incorporation 2.0h after release into S phase. Although, across the genome, H3.3 was still broadly enriched at early-replicating regions, loss of HIRA had two effects (Figure 7A). First, in regions of broad H3.3 enrichment, boundaries became blurred and separate peaks dissolved into larger domains (blurred sites). Second, a number of H3.3 peaks disappeared entirely or became enriched in H3.1 (buried sites). Notably, in both cases, replication changed accordingly. At sites that became blurred, we found fuzzy replication patterns as shown by diffuse EdU incorporation. More strikingly, at buried sites, HIRA loss led to the complete abrogation of early replication zones (red marks, Figure 7A), with a clear EdU depletion indicative of either a loss or significant delay in origin firing. Remarkably, we found these effects across all H3.3 sites with detectable EdU signal (Figure 7B). ~3000 sites (Table S2) were still enriched in EdU after HIRA knockout (EdU^{+} blurred sites, Figure 7B top panels). However, as H3.1 and H3.3 became diluted in HIRA^{KO} cells, fuzzy initiation patterns emerged across all sites (Figure 7B, HIRA^{KO} top panels). In parallel, we detected ~600 buried sites (Table S2) with a significant EdU depletion after HIRA loss (EdU^{-} buried sites, Figure 7B bottom panels). In the absence of HIRA, both H3.3 and EdU became depleted, with many early IZ showing no detectable EdU incorporation or disappearing entirely (Figure 7B, HIRA^{KO} bottom panels). To deepen our analysis of the HIRA knockout, we further compared transcription and PTM patterns between H3.3 sites that became either blurred or buried. We found that blurred sites correspond to active transcription units (Figure S6A, top panels). In contrast, we located buried sites in regions of low transcriptional activity or with no detectable RNA signal (RNA track in Figure 7A, and Figure S6A bottom panel). This is further reflected by low or undetectable RNA Pol II signal and absence of active turnover marks (Figure S6A bottom panels). Hence, without transcription, the loss of HIRA completely abolished H3.3 targeting and buried sites no longer replicated in early S phase. In contrast, deposition sites coupled to transcription only lost the precise H3.3 targeting, with fuzzy replication patterns emerging across their boundaries. Importantly, we observed a comparable effect when probing *de novo* H3.1 deposition in H3.1-SNAP HIRA^{KO} cells

(Figure S6B). Since H3.1 deposition tracked fork progression in early S (Figure 2 and 3), this further demonstrated that the deletion of HIRA had a systematic effect on early replication patterns. We thus conclude that HIRA is critical for the stable location of replication zones and to ensure early origin firing at IZ across H3.1/H3.3 boundaries, with a strict requirement at regions that are not transcriptionally active.

Discussion

Distinct deposition of H3.1 and H3.3 during S phase demarcates the initiation zones of early origins

Here, by tracking *de novo* H3.1 and H3.3 at genome-wide resolution in synchronized cells (Figure 1), we investigated how their distinct deposition impacts the replication program. We found that, while new H3.1 deposition follows S phase progression and dynamically spreads along the genome, new H3.3 is exclusively re-targeted to sites where there is preexisting H3.3. Concomitantly with S phase progression, these two concurrent mechanisms produce a stable partitioning between sites of H3.3 deposition, coupled to turnover, and the intervening boundaries, where H3.1 is deposited in early S phase. These boundaries thus mark the IZ of early-firing origins (Figure 5C) and can already be identified in G1/S prior to DNA synthesis. We propose that the distinct deposition of H3.1 and H3.3 plays a major role in preserving IZ at the boundary between histone variants. Of note, the number of H3.1/H3.3 boundaries that we detect in G1/S cells (~6000 around each H3.3 site, cf. Figure 5A) is comparable to the number of IZ found in asynchronous cells by optical replication mapping (~5000 IZ, Wang et al., 2021). Importantly, we show that perpetuation of these boundaries is under the control of the HIRA pathway for H3.3 deposition. Indeed, deletion of the HIRA chaperone prevents H3.3 deposition at pre-marked sites during DNA synthesis, leading to the disruption of H3.1/H3.3 boundaries, and altering patterns of origin firing throughout the genome. In these conditions, we distinguish two scenarios. In transcribed regions, boundaries became blurred and replication initiation occurred diffusely, reflecting a loss of precision in the locations of origin firing. More strikingly, in low-transcribed or inactive regions, a complete erasure of boundaries occurred (buried sites) with abrogation of early initiation. This finding is particularly striking to further emphasize that early IZ are not merely a consequence of transcription. We conclude that HIRA plays a critical role in the definition of early replication zones both in transcribed and non-transcribed regions.

H3.1/H3.3 boundaries partition the genome to coordinate replication with transcription

By targeting new H3.3 at defined locations, HIRA produces a precise transition between H3.1 deposited with replication and H3.3 deposited with turnover. Thus, the boundary between both variants maintains a stable trace of initiation events, marking their location systematically. In addition, while H3.3 deposition can be coupled to transcription, we also found it at non-transcribed regions. Hence, this mechanism provides a marking system to preserve IZ independent of transcription itself. The close relationships between replication and transcription has long been acknowledged in viral systems (DePamphilis, 1988) and supported by genome-wide analyses in mammalian cells (Hansen et al., 2010; Petryk et al., 2016; Chen et al., 2019). This is best illustrated by the reshaping of the replication program along with changes in transcription as pluripotent cells undergo differentiation (Hiratani et al., 2008; Hiratani et al., 2010; Rivera-Mulia et al.,

2015; Rausch et al., 2020) and during embryo development (Hyrien and Méchali 1993; Hyrien et al., 1995; Sasaki et al., 1999; Siefert et al., 2017). Accordingly, transcriptional reprogramming is accompanied by dynamic changes in H3.3 distribution (Yadav et al., 2018). However, the question remained whether it was the act of transcription itself that could drive the replication program or other mechanisms. To date, the link between H3 variant deposition and DNA replication had not been considered. While HIRA can target H3.3 in a manner coupled to transcription, our results also highlight a unique and unexpected role in shaping the early replication program in both transcribed and non-transcribed regions. A model thus emerges whereby, in differentiating cells, H3.3 deposition could favor replication initiation in proximity of newly activated genes and, in turn, *de novo* H3.1 deposition by CAF-1. This distinct deposition can thus provide a mechanism for partitioning the epigenome to coordinate replication and transcription, which may help minimize conflicts between RNA and DNA polymerases (Lin and Pasero, 2012; Promonet et al., 2020). We propose that, while H3.1 is incorporated ubiquitously with fork progression, HIRA maintains the positioning of early replication zones by targeting new H3.3 to replace H3.1 within their boundaries. Hence, the boundaries selectively mark the locations of IZ where H3.1 deposition starts in early S phase, without being replaced by new H3.3. The retention of H3.1 at the flanks of high-turnover regions is consistent with its patterns of recycling on replicating DNA, where old H3.1 is retained at inactive loci but not at active ones (Escobar et al., 2019). This could provide a fallback mechanism to preserve diffuse boundaries at blurred sites, where H3.1 loss would still occur with transcription (Torné et al., 2020) even in the absence of H3.3 replacement. In contrast, without HIRA or transcription, buried sites become homogeneously covered with H3.1 and boundaries disappear completely. Understanding what drives HIRA recruitment at these sites, and which pathways compensate for its loss, are exciting avenues of investigation to illuminate how histone dynamics shape early replication zones. A follow-up question is whether H3.1 and H3.3 themselves have a role in replication initiation. Interestingly, H3.1 and H3.3 variants are conserved in most eukaryotes (Waterborg et al., 2012) with the exception of budding yeast, where origins are sequence-dependent (Prioleau and MacAlpine, 2016). One could envisage that each variant, with its specific post-translational modifications, can attract or repel specific factors, which may in turn favor or prevent origin firing. Indeed, replication origins are enriched in active marks typical of promoters and enhancers (Cayrou et al., 2015; Miotto et al., 2016) but ORC components associate preferentially with repressive methylated forms (Vermeulen et al., 2010). The presence of both H3 variants may thus provide a unique scaffold for recruiting factors that recognize different marks or other associated variants, such as H2A.Z (Martire and Banaszynski, 2020). A key question, in this respect, is the effect of H3.3 serine 31 phosphorylation (S31P), which is the only residue that can discriminate the tail of the two variants. H3.3 S31P can promote K27 acetylation both in *cis* (Sitbon et al., 2020) and in *trans* (Martire et al., 2019). This capacity to modulate PTMs may be important to promote initiation as seen, for instance, for the histone H3 demethylase KDM4 (Wu et al., 2017). Furthermore, by facilitating or preventing contacts at distant loci that participate in higher-order chromatin organization (Sima et al., 2019), the presence of distinct variants may also contribute to the control of replication timing. Interestingly, while recent work has proposed that replication timing organizes the epigenomic landscape (Klein et al., 2021), our results show that the deposition of distinct variants has an impact on the replication program. This opens up

exciting avenues for histone variants as key players in crosstalk with replication factors to shape genome organization at different scales.

HIRA shapes the early replication program: implications for cell fate in development and disease

The distinct partitioning of H3.1 and H3.3 during DNA replication preserves a genome-wide footprint which could also be relevant to maintain cell identity. Since previous RNAi screens identified subunits of the CAF-1 complex as key factors for safeguarding cell identity in fibroblasts (Cheloufi et al., 2015), the respective roles of HIRA and CAF-1 should be considered in this context. Furthermore, in non-tumorigenic cells, the acquisition of aggressive traits by epithelial-to-mesenchymal transition involves CAF-1 inactivation accompanied by H3.3 deposition via HIRA to promote a global reprogramming (Gomes et al., 2019). HIRA is also critical during early development, with several studies exploring the connection between H3.3 deposition and zygotic transcriptional activation (Filipescu et al., 2014). Even in the absence of transcription, H3.3 incorporation can sustain an epigenetic memory of active gene states (Ng and Gurdon, 2008) which may either act as a barrier to reprogramming, like H3K4 methylation during nuclear transfer (Hörmanseder et al., 2017), or facilitate the activation of lineage-specific genes, as for H3K27 acetylation in pluripotent stem cells (Pelham-Webb et al., 2021). Based on our findings, we put forward a role for HIRA in replication, which would similarly operate independently of transcription. This may explain previous observations in mouse embryos that showed that HIRA deletion impaired DNA replication and prevented development past the zygotic stage (Lin et al., 2014). In the context of cancer, the recurrence of both H3.1 and H3.3 "oncohistone" substitutions has been associated with a capacity to lock cells in a state refractory to differentiation (Nacev et al., 2019). In this respect, it is interesting to note that the effect of H3.1 or H3.3 oncohistones is dependent on their specific deposition pathway (Sarthy et al., 2020). Furthermore, cancer cells divide indefinitely and cope with additional DNA damage and replication stress. Patterns of origin firing change in conditions of replicative stress (Macheret and Halazonetis, 2018) and in the presence of DNA damage (Yekezare et al., 2013). Since HIRA promotes transcriptional reactivation after DNA repair (Adam et al., 2013), it is tempting to speculate that H3.3 deposition at damaged sites rewires early replication patterns and helps cancer cells adapt to stress conditions. This may also elucidate why H3.3 is dispensable for replication in *D. melanogaster* under normal conditions (Paranjape and Calvi, 2016) and is only required for proper replication under temperature stress in *C. elegans* (Strobino et al., 2020). How histone chaperones shape the replicating genome is hence a crucial avenue of investigation, which may have profound implications for how the chromatin landscape adapts to programmed changes in cell fate or to cope with stress conditions.

In conclusion, how to specify a replication origin in mammals remains a major challenge. Series of studies have proposed various possibilities, implicating genomic and epigenomic features that largely relate to transcription (Fragkos et al., 2015; Marchal et al., 2019). Considering boundaries between H3.1 and H3.3, and the importance of histone replacement within early replication zones, could provide a unifying framework. Indeed, the deposition of distinct variants is not only critical for chromatin assembly during DNA replication, or a mere reflection of transcription: it has a direct impact on replication itself.

Limitations of the study

Our results show that the HIRA pathway maintains early replication zones by promoting the targeted replacement of H3.1 with new H3.3. However, the link between specific variants and replication initiation remains to be explored. Future studies can help illuminate whether the identity of each variant is critical, or only the systematic targeting of newly synthesized histones to replace those deposited with the replication fork. The role of histone recycling, or deposition pathways that may compensate for HIRA loss, are also important avenues of investigation. Finally, additional methods to probe the effect of HIRA loss on replication (e.g. OK-Seq, high-resolution Repli-Seq or optical replication) will help understand whether H3.1/H3.3 boundaries directly affect replication initiation, or merely dictate the timing and localization of early replication zones.

Our work opens new avenues to investigate how this is operating at a molecular level, or link to 3D genome architecture. We hope that this will pave the way for exciting discoveries bridging chromatin dynamics and genome function.

Acknowledgements

We thank Daniel Jeffery for critical reading of the manuscript, Guillermo A. Orsi for help at the initiation of the project, the Cell and Tissue Imaging Platform - PICT-IBiSA (member of France-Bioimaging ANR-10-INBS-04) of the UMR3664 and ICGex NGS platform of the Institut Curie. A.G. was supported by individual funding (H2020 Marie Skłodowska-Curie Actions grant agreement 798106 "REPLICHROM4D") and ERC-2015-ADG-694694 "ChromADICT". This work was supported by the ERC-2015-ADG-694694 "ChromADICT" and the Ligue Nationale contre le Cancer (Equipe labellisée Ligue). It benefited from ANR-11-LABX-0044_DEEP and ANR-10-IDEX-0001-02 PSL; ANR-14-CE10-0013 "CELLECTCHIP" and ANR-16-CE12-0024 "CHIFT".

Author contributions

Conceptualization, G.A. and J.-P.Q.; Methodology, A.G., A.F., J.-P.Q. and G.A.; Software, A.G.; Validation, A.G., A.F., J.-P.Q. and G.A.; Formal Analysis, A.G., A.F., J.-P.Q. and G.A.; Investigation, A.G., A.F., J.-P.Q.; Data Curation, A.G.; Writing - Original Draft, A.G., A.F., J.-P.Q. and G.A.; Writing - Review & Editing, A.G., J.-P.Q. and G.A.; Visualization, A.G., J.-P.Q. and G.A.; Supervision, J.-P.Q. and G.A.; Project Administration, G.A.; Funding Acquisition, G.A.

Declaration of Interests

The authors declare no competing interests.

Main figures

Figure 1. Cell synchronization coupled to SNAP capture to track new H3.1 and H3.3 along S phase

A. Scheme of quench-chase-capture strategy to selectively track new H3.1 and H3.3 during S phase. Cells constitutively expressing H3.1- or H3.3-SNAP are first synchronized in G1/S via double-thymidine block. The SNAP-tag of existing histones is rendered non-reactive by covalent binding of a cell-permeable benzylguanine derivative (SNAP block). The SNAP block is added to the medium for 2.0h (quench), then an additional 0.5h is allowed for synthesis of new histones with a reactive SNAP-tag (chase). After quench and chase, thymidine is washed from the medium and cells are released into S phase. Native mononucleosomes are purified by MNase digestion at consecutive time points after release, and newly deposited H3.1/H3.3 (with a reactive SNAP-tag) are isolated with SNAP capture beads.

B. Representative images showing DNA synthesis (EdU, green) and *de novo* H3.1 and H3.3 (TMR, red) patterns in the nucleus (DAPI, blue) after quench-chase-pulse labeling in synchronized cells at 0.0h, 2.0h and 5.0h after release into S phase. At 2.0h, early S phase patterns are prevalent, and most cells show broad EdU and TMR labeling in the nucleus (95.6% ± 5 of H3.1-SNAP cells and 93.0% ± 2 of H3.3-SNAP cells, over three acquisitions with n = 100 cells). Instead, at 5.0h, most cells exhibit mid S phase patterns with EdU around the nucleolus and at the nuclear periphery (83.6% ± 6 of H3.1-SNAP cells and 84.2% ± 3 of H3.3-SNAP cells, over three acquisitions with n = 100 cells). In replicating cells, new H3.1 is consistently enriched at EdU foci, while new H3.3 shows a diffuse localization independent of S phase progression. Scale bars represent 10 μm.

See also Figure S1

Figure 2. New H3.1 deposition spreads with fork progression during S phase, while new H3.3 is systematically deposited at preexisting sites

A. Experimental design for tracking *de novo* H3.1 (left) and H3.3 (right) deposition at genome-wide resolution during S phase, relative to their preexisting distribution. Total H3.1 and H3.3 are profiled by SNAP capture sequencing in synchronized cells at the time of release (G1/S). New H3.1 and H3.3 are isolated at 2.0h and 5.0h post release, following a 2.0h quench (to prevent the capture of preexisting histones) and 0.5h chase (to allow for the synthesis of new H3.1 or H3.3 with a reactive SNAP-tag). For all samples, input DNA after MNase digestion was sequenced in parallel as a control.

B. The replication timing from early (S_1) to late S phase (S_6) is shown for reference at a representative region of chromosome 18 (q11.2 to q21.1), based on Repli-Seq data from Dellino et al., 2013. The tracks show the relative proportion of BrdU incorporation in each S phase fraction, at consecutive bins of 10 kb (counts per million in a given fraction relative to maximum across all fractions, smoothed over 3 non-zero bins).

C. Distribution of total H3.1 in G1/S (top track) and newly deposited H3.1 at 2.0h and 5.0h after release into S phase (bottom tracks). Each track shows H3.1 enrichment relative to input (counts per million, z-transformed $\log_2$ ratio) at bins of 10 kb, smoothed over 3 non-zero bins. Enriched and depleted bins are highlighted in different colors (dark purple for enriched, light purple for depleted).

D. Total and *de novo* H3.3 patterns in G1/S and at 2.0h and 5.0h after release are similarly shown in dark green (enriched) and light green (depleted).

E. Mean H3.1 and H3.3 enrichment at regions of 10 kb throughout the genome, ranked by replication timing from early to late (S_1 to S_6) based on the peak of DNA synthesis. Each region is assigned to the S phase fraction showing the maximum BrdU incorporation then, for each sample, the mean enrichment and 95% CI is computed across all regions assigned to a given fraction. Total and *de novo* H3.1 and H3.3 trends are respectively shown in purple (top panels) and green (bottom panels), at different time points along S phase (G1/S, 2.0h and 5.0h after release).

See also Figure S2

Figure 3. H3.3 sites are delimited by H3.1-rich boundaries where new H3.1 is deposited with early DNA synthesis

A. Total and *de novo* H3.3 enrichment at preexisting H3.3 sites along S phase progression (n = 2926 locations where H3.3 is the prevalent variant in G1/S cells, filtered based on enrichment relative to input at 10% FDR).

B. Total and *de novo* H3.1 enrichment trends are similarly shown at the same sites. For each sample, the color gradient is proportional to its enrichment relative to input ($\log_2$ ratio, z-transformed) at bins of 10 kb around the center ± 0.5 Mb. The average trend is shown below, in green for H3.3 and purple for H3.1 (mean enrichment across all sites and 95% CI).

C. Patterns of DNA synthesis across all H3.3 sites, based on Repli-Seq data from Dellino et al., 2013. The heat maps show relative BrdU incorporation from early to late S phase (counts per million in a given fraction, normalized to the maximum across all fractions) at bins of 10 kb around the center of each site ± 0.5 Mb. The average trend is shown below (mean and 95% CI).

   In all plots, the y-axis range is the same as the color gradient (indicated in the corresponding color bar).

See also Figure S3

Figure 4. The distinct deposition of H3.1 and H3.3 across existing boundaries occurs both with or without transcription

A. H3.3 enrichment before (total H3.3, G1/S) and after release into S phase (new H3.3, 2.0h) compared to replication timing (Repli-Seq data, Dellino et al., 2013) and transcription (nascent RNA-Seq data,

Liang et al., 2015) at a selected region on chromosome 13 (q14.12 to q21.31). The tracks show H3.3 enrichment relative to input (counts per million, z-transformed $\log_2$ ratio), BrdU incorporation from early to late S phase (counts per million in a given S phase fraction relative to maximum across all fractions) and nascent RNA from asynchronous cells ($\log_2$ counts per millions) at consecutive bins of 10 kb, smoothed over 3 non-zero bins. H3.3-rich or depleted bins are highlighted in different colors (dark green for enriched, light green for depleted).

B. H3.3 and H3.1 enrichment before (total, G1/S) and after release into S phase (*de novo*, 2.0h) around H3.3 sites that are actively transcribed (RNA^+, top 95%) or low- to non-transcribed (RNA^-, bottom 5%). H3.3 sites detected from G1/S cells (n = 2926, 10% FDR) were divided at the 5^{th} percentile based on nascent RNA-Seq counts (Liang et al., 2015), averaged at 10 kb resolution from start to end position. For both RNA^+ and RNA^- sites, the heat maps show the nascent RNA signal ($\log_2$ counts per million), total H3.3 and H3.1 at G1/S and *de novo* H3.3 and H3.1 and 2.0h ($\log_2$ ratio to input) at bins of 10 kb around the center ± 0.5 Mb, z-transformed across all sites. The average trend shown below (mean and 95% CI) is displayed in red for nascent RNA, green for H3.3 and purple for H3.1. The y-axis range is the same as the color gradient (indicated in the corresponding color bar).

See also Figure S4

Figure 5. H3.3 sites are replicated by early-firing forks converging from initiation zones at the H3.1-rich boundaries

A. H3.1 and H3.3 enrichment around H3.3-rich ($H3.3^+$ IZ, top) or H3.3-poor initiation zones ($H3.3^-$ IZ, bottom) from OK-Seq data (Petryk et al., 2016) compared to early firing patterns (EdU HU^+, EdU-HU-Seq data from Macheret and Halazonetis, 2018). IZ were identified by fitting a 2-states HMM on replication fork directionality (RFD), computed at 10 kb resolution using both EdC replicates from Petryk et al., 2016. IZ were assigned to the location where rightward-moving forks (red) diverge from leftward-moving forks (red), and classified in H3.3-rich or H3.3-poor based on average enrichment in a 100 kb window around each location ($H3.3^+$ if $\log_2$ ratio to input > 0, $H3.3^-$ if $\log_2$ ratio to input < 0). For both $H3.3^+$ and $H3.3^-$ IZ, the heat maps show the RFD for each EdC replicate, H3.3 and H3.1 enrichment ($\log_2$ ratio to input, z-transformed) and the EdU signal after HU treatment ($\log_2$ counts per million, z-transformed) at bins of 1 kb around each IZ ± 0.2 Mb. We ranked IZ by initiation efficiency based on the amplitude of the RFD shift, averaged between both replicates (ΔRFD). The average trend is shown below (mean and 95% CI) in red and blue for RFD, green for H3.3, purple for H3.1 and blue for EdU. The y-axis range is the same as the color gradient and shown in the corresponding color bar, except for the RFD signal where the y-axis range is [-0.5, +0.5].

B. Replication initiation patterns relative to H3.1 and H3.3 distribution in G1/S cells, based on available OK-Seq (Petryk et al., 2016) and EdU-HU-Seq data (Macheret and Halazonetis, 2018). The heat maps show the respective signal at 10 kb bins around the center of H3.3 sites ± 0.5 Mb. The

replication fork directionality (RFD) measures the difference between Okazaki fragments from the Crick strand (rightward-moving forks, red) and the Watson strand (leftward-moving forks, blue) ranging from -1 (leftward-moving forks only) to +1 (rightward-moving forks only). The EdU HU^+ signal reflects early origin firing as measured by EdU incorporation after HU treatment (log_2 counts per million, z-transformed). For each sample, the average trend is shown below (mean across all sites and 95% CI). In all plots, the y-axis range is the same as the color gradient (indicated in the corresponding color bar) except for the mean RFD signal, where the y-axis range is [-0.2, +0.2].

In each panel, H3.1/H3.3 profiles are shown from different viewpoints with heat maps in panel A centered at initiation zones, and in panel B in the middle of each H3.3 site. These two complementary viewpoints show opposite patterns but reflect the same distribution. Early IZ ($H3.3^+$) overlap the H3.1-rich boundary separating H3.3 sites, where H3.1 peaks at the center and H3.3 at the flanks (panel A, top). These narrow H3.1 peaks delineate the two boundaries of each H3.3 site, where early forks diverge from IZ on both sides and converge midway (panel B).

C. Scheme illustrating the establishment of H3.1/H3.3 boundaries at early replication zones. H3.1 deposition tracks fork progression starting from the boundaries of H3.3 sites (DNA synthesis-coupled deposition, DSC), where H3.3 is systematically targeted independent of H3.1 or fork progression (DNA synthesis-independent deposition, DSI). H3.3 can thus replace H3.1 deposited with fork progression at preexisting sites, where H3.1 is only retained at the boundaries. This dual deposition mechanism thus maintains boundaries at the same location, producing a stable footprint of fork progression in early S phase and marking the location of early IZ.

See also Figure S5

Figure 6. HIRA deletion impairs H3.3 deposition and delays S phase entry without affecting fork speed

A. *De novo* H3.3 deposition during early S phase in H3.3-SNAP $HIRA^{WT}$ and $HIRA^{KO}$ cells, at 2.0h after release from double-thymidine block. In both cell lines, the heat map shows the enrichment in newly deposited H3.3 (log_2 ratio to input, z-transformed) at bins of 10 kb around the center of all H3.3 sites detected in the parental cell line ± 0.5 Mb. The mean enrichment and 95% CI is shown below, the y-axis range is the same as the color gradient.

B. Proportion of replicating cells in $HIRA^{WT}$ and $HIRA^{KO}$ at 2.0h and 5.0h after release into S phase. The bar plot shows the mean percentage of EdU^+ cells in $HIRA^{WT}$ (dark blue) and $HIRA^{KO}$ (light blue) cells, H3.1-SNAP or H3.3-SNAP (mean and standard deviation over a minimum of five independent experiments, each counting over a total of n = 100 cells cf. Table S1).

C. S phase progression in $HIRA^{WT}$ and $HIRA^{KO}$, based on patterns of EdU localization at 2.0h and 5.0h after synchronization and release. The bar plots show the mean percentage of early, mid and late S cells at 2.0h and 5.0h, estimated by EdU labeling in $HIRA^{WT}$ (right) and $HIRA^{KO}$ (left) H3.1- or

H3.3-SNAP cell lines (mean and standard deviation in two independent experiments, with at least = 400 cells pooled over multiple acquisitions cf. Table S1).

D. Comparison of replication fork speed by DNA combing in H3.3-SNAP HIRA^{WT} and HIRA^{KO}. Fork speed was estimated in kilobase per minute using all fibers where two converging (termination) or diverging forks (initiation), or a unidirectional fork, could be detected after two consecutive CldU (red) and IdU (green) pulses of 0.5h. A representative image is shown in the right panel. The box plots show the distribution of replication fork speeds in two replicates (x-axis) for both HIRA^{WT} (dark blue) and HIRA^{KO} cells (light blue), either asynchronous or 1.0h after release from double-thymidine block.

p-values were calculated by two-tailed Mann–Whitney U test (differences in proportions between HIRA^{WT} and HIRA^{KO} cells, panel B and C) and two-tailed Welch's t-test (differences in fork speed, panel D) and indicated on the respective panels: ns ($p > 0.05$), ** ($p < 0.01$), *** ($p < 0.001$). All differences proved significant after Bonferroni correction (cf. Table S1).

Figure 7. HIRA deletion disrupts H3.1/H3.3 boundaries leading to diffuse replication in active regions and abrogation of early replication zones in non-transcribed regions

A. Differential H3.3 to H3.1 content in G1/S compared to early initiation patterns in HIRA^{WT} and HIRA^{KO} cells, along a representative region of chromosome 15 (q24.3 to q26.3). The H3.3 to H3.1 ratio shows the prevalence of a given variant in G1/S (difference-sum ratio between H3.3- and H3.1-SNAP counts per million) from -1 (only H3.1) to +1 (only H3.3). The ratio is computed at bins of 10 kb, bins are colored in green if H3.3 is prevalent (positive values) or purple if H3.1 is prevalent (negative values). In wild type and knockout cells, the G1/S profile of both variants is compared to EdU enrichment at 2.0h into S phase (log_2 ratio to input, z-transformed) after a 0.5h pulse in synchronized H3.3-SNAP cells. Bins enriched in EdU are colored in blue, depleted bins in grey. Patterns of transcriptional activity across the region are shown for reference on the bottom, based on nascent RNA-Seq data from Liang et al., 2015 (log_2 counts per million at 10 kb resolution). In HIRA^{KO} cells, H3.1/H3.3 boundaries and early replication zones are disrupted. In actively transcribed regions, boundaries are lost and separate peaks dissolve into broader domains of diffuse initiation (blurred sites). Instead, in non-transcribed regions, H3.3 peaks disappear and initiation is either impaired or fully abrogated (buried sites). The location of buried sites is indicated in red above each track. We detected H3.3 sites via a 3-state HMM in HIRA^{WT} cells at G1/S, and filtered based on EdU enrichment at 2.0h (one-tailed binomial test, 10% FDR). We classified sites with significant EdU enrichment in HIRA^{KO} cells as "blurred", those with significant EdU depletion as "buried" (two-tailed binomial test, 10% FDR).

B. Genome-wide patterns of H3.3, H3.1 and EdU enrichment at blurred and buried sites in HIRA^{WT} (right) and HIRA^{KO} cells (left). For both blurred (EdU^{+}, top row) and buried sites (EdU^{-}, middle row), the heat maps show H3.3 and H3.1 enrichment in G1/S compared to EdU incorporation 2.0h after release into S phase (log_2 ratio to input, z-transformed) at bins of 10 kb around the center of

each site ± 0.5 Mb. The bottom panel shows the mean enrichment and 95% CI across all blurred sites (solid lines with darker shades) and buried sites (dotted lines with lighter shades). The y-axis range is the same as the color gradient.

See also Figure S6

STAR Methods

RESOURCE AVAILABILITY

Lead Contact

Further information and requests for resources and reagents should be directed to and will be fulfilled by the lead contact, Geneviève Almouzni (genevieve.almouzni@curie.fr).

Materials availability

All unique materials and reagents generated in this study are available from the lead contact upon request.

Data and Code availability

- Sequencing data from SNAP and EdU capture assays have been deposited in ArrayExpress under accession number E-MTAB-10619. Accession numbers for all sequencing runs from publicly available data are listed in Table S4. Raw images for Figure 1A, Figure 6D and Figure S1D have been deposited at Mendeley Data (DOI: 10.17632/8zzsz58kgg.2). Source data for all image quantification analyses are provided in Table S1.
- This paper does not report original code
- Any additional information required to reanalyze the data reported in this paper is available from the lead contact upon request.

EXPERIMENTAL MODEL AND SUBJECT DETAILS

Cell lines

We used HeLa cells stably expressing H3.3-SNAP-HA or H3.1-SNAP-HA (parental cell lines), HIRA knockout cells ($HIRA^{KO}$: H3.3-SNAP-HA HIRA CRISPR/Cas9 KO and H3.1-SNAP-HA HIRA CRISPR/Cas9 KO) and HIRA wild-type control cells ($HIRA^{WT}$: H3.3-SNAP-HA GFP CRISPR/Cas9 KO and H3.1-SNAP-HA GFP CRISPR/Cas9 KO) as in Ray-Gallet et al., 2018. We cultured cells in DMEM complete medium (Dulbecco's Modified Eagle's Medium with D-Glucose, L-Glutamine and Pyruvate) supplemented with 10% fetal calf serum, 100 U/mL Penicillin and 100 μg/mL Streptomycin. All cell lines tested negative for mycoplasma contamination.

METHOD DETAILS

Cell synchronization and SNAP-tag quench-chase strategy

To probe deposition patterns during S phase, we grew cells in 15 cm Petri dishes, synchronized in G1/S via double thymidine block: sequential exposure to 2 mM thymidine (16-18h), 24 μM 2-Deoxycytidine (6h) and 2 mM thymidine (18h). To selectively track newly synthesized H3.1- and H3.3-SNAP, we quenched the SNAP-tag of parental (old) histones by exposing G1/S cells to 10 μM SNAP-Cell Block (S9106S, New England Biolabs) for 30 minutes, followed by 2 hours chase (cells incubated in media without SNAP-Cell Block but containing 2 mM thymidine). We released cells into S phase by three PBS washes and incubation

in DMEM complete medium supplemented with 24 µM 2-Deoxycytidine. We collected samples at consecutive time points after release into S phase (2.0h and 5.0h). In parallel, we collected H3.1- and H3.3-SNAP at the time of release (0.0h) without previously adding SNAP-Cell Block to the medium (no quench) to probe for total H3.1- and H3.3-SNAP in G1/S.

Microscopy

To monitor DNA synthesis, H3.1 and H3.3 incorporation in live cells, we used cells grown on coverslips laid in Petri dishes, and performed EdU, H3.3- and H3.1-SNAP labeling *in vivo* as in Clément et al., 2018. For H3.1- and H3.3-SNAP labeling, we added 6 µM SNAP-Cell TMR-Star (S9105S, New England Biolabs) for 20 minutes for total H3.1- or H3.3-SNAP histones (absence of block) or 30 minutes when probing new histones after quench-chase. Following SNAP-TMR and EdU labeling, and extraction with Triton-CSK prior to cell fixation, we proceeded with EdU detection using Click-iT EdU Cell Proliferation Kit for imaging, Alexa Fluor 488 dye (C10337, Thermo Fisher) and DAPI staining. We used a Zeiss Imager Z1 epifluorescence microscope with MetaMorph software, 63X and 40X Oil Objective lenses and an ORCA-Flash4.0 LT camera (Hamamatsu) for image acquisition.

Native nucleosome isolation

We harvested asynchronous or G1/S synchronized cells by trypsinization and counted them with an automated cell counter (Vi-CELLXR, Beckman). We collected four million cells, washed with PBS and pelleted by centrifugation in low adhesion tubes. We processed one million cells at a time, resuspended the cell pellet in 100 µL lysis buffer (50 mM Tris–HCl pH 7.5, 150 mM NaCl, 5 mM CaCl2, 1% Triton X-100, 0.5% NP40 and cOmplete™ EDTA-free protease inhibitor cocktail by Roche) and incubated for 4 minutes at room temperature (RT). After centrifugation (5 min, 500 ×g) we eliminated the cytosolic fraction and resuspended the pelleted chromatin fraction in 25 µl lysis buffer. We then added 3U MNase (EN0181, ThermoScientific) and incubated for 8 minutes at 37°C. We stopped digestion by addition of EGTA to 20 mM. After 10 minutes incubation on ice we centrifuged 10 minutes at 10000 ×g. We resuspended the pellet with the supernatant to extract soluble nucleosomes and proceeded to a second 10 minutes 10 000 ×g centrifugation. We recovered the supernatant containing the native nucleosomes in low adhesion tubes, and added 5 volumes of binding buffer (50 mM Tris–HCl pH 7.5, 100 mM NaCl, 1 mM DTT, 0.5% BSA and cOmplete™ EDTA-free protease inhibitor cocktail by Roche). We kept samples on ice prior to SNAP capture and sequencing.

SNAP capture and sequencing (SNAP-Seq)

We prepared SNAP-Capture magnetic beads (S9145S, New England Biolabs) by washing and coating for 1 hour in coating buffer (PBS, 2.5% BSA, 0.05% Tween 20). We mixed 10 µl of SNAP-Capture magnetic beads with the native nucleosomes (input) and incubated overnight at 4°C on a rotating wheel. We collected beads with a magnetic rack, discarded supernatant and washed beads in 1 mL, twice with wash buffer 1 (10 mM Tris–HCl pH 8, 140 mM NaCl, 1% Triton X-100, 0.5% NP40, 0.1% SDS), twice in wash buffer 2 (10

mM Tris–HCl pH 8, 360 mM NaCl,1% Triton X-100, 0.5% NP40, 0.1% SDS), twice in wash buffer 3 (10 mM Tris–HCl pH 8, 250 mM LiCl, 0.5% Triton X-100, 0.5% NP40) and twice in TE buffer (10 mM Tris–HCl pH 8.0, 1 mM EDTA). Finally, we resuspended the beads in 20 µl TE and released DNA from bound nucleosomes by RNAse digestion (2 µl RNase A, 1 µg/µl, 30 min at 37°C) and subsequent proteinase K digestion in the presence of SDS (2 µl proteinase K, 20 µg/µl, and 2.5 µl SDS 20%, 2 hours at 37°C). Beads were removed by magnetic separation and DNA extracted using Agencourt AMPure XP Beads (A63880, Beckman Coulter), according to the manufacturer's instructions, and eluted in 20 µl water. After checking the purified DNA profile (Agilent 4200 TapeStation), we prepared sequencing libraries at the Next Generation Sequencing (NGS) platform from Institut Curie using the Illumina TruSeq ChIP kit, and paired-end sequenced on Illumina HiSeq 2500 (samples from parental cell lines) or Illumina NovaSeq 6000 (samples from $HIRA^{WT}$ and $HIRA^{KO}$ cell lines).

Nascent DNA purification and sequencing (EdU-Seq)

We labeled nascent DNA by adding EdU (25 µM) for 30 minutes. After 2 washes in PBS, 8 million cells were harvested by trypsinization. We next lysed the cells in low adhesion tubes by 4 minutes incubation at RT in 500 µl lysis buffer (50 mM Tris–HCl pH 7.5, 150 mM NaCl, 5 mM CaCl2, 1% Triton X-100, 0.5% NP40 and cOmplete™ EDTA-free protease inhibitor cocktail by Roche) and collected the chromatin fraction by centrifugation for 5 minutes at 500 ×g. After removal of the supernatant, we next "clicked" the cleavable biotin linker (Biotin-PEG3-SS-azide, BP-22955, BroadPharm) onto EdU by resuspending the lysed nuclei pellet in 300 ul Click-iT buffer, CuSO4 reaction additive, according to manufacturer's instructions (Thermo Fisher). After 25 minutes incubation at RT in the dark, we recovered chromatin by centrifugation, washed with lysis buffer and processed for MNase, RNase then Proteinase K digestion as above (native nucleosome extraction). We extracted DNA from native nucleosomes by phenol-chloroform and ethanol precipitation and resuspended the DNA pellet in 100 ul H2O (input. We recovered biotinylated EdU-labeled fragments with 33 µl of Dynabeads M-280 Streptavidin (11205D, Thermo Fisher) by 15 minutes incubation at RT on rotating wheel and subsequent washes according to manufacturer's instructions. We eluted bead-bound DNA by cleaving the S-S bond with a 1 h incubation at RT in TE buffer supplemented with 2% β-mercaptoethanol. Finally, we purified released DNA by phenol-chloroform extraction, EtOH precipitation and resuspended in 20 µl water. After checking the purified DNA profile (Agilent 4200 TapeStation), we prepared sequencing libraries as above.

Sequencing data analysis

We processed both samples from in-house and published experiments from raw reads in FASTQ format, except for input-normalized tracks from ENCODE project that were batch downloaded via the ENCODE Portal (https://www.encodeproject.org). We aligned reads to the human reference genome (GRCh38, soft-masked assembly) with Bowtie 2 (version 2.3.4.2, Langmead and Salzberg, 2012) with --very-sensitive parameters. For RNA-Seq data, we aligned reads with HISAT2 (version 2.1.0, Kim et al., 2019) with default parameters, using Ensembl gene annotations (release 95). Duplicate alignments were flagged using

SAMtools (version 1.9, Danecek et al., 2021) after sorting and indexing the corresponding BAM file. For each sample, we computed read counts (for single-end data) or fragment counts (for paired-end data) from primary alignments, excluding duplicates, at consecutive bins of 1 kb using BEDTools (version 2.27.1, Quinlan and Hall, 2010). We then aggregated counts at 10 kb resolution, normalized to the total number of mapped reads or fragments per sample (counts per million, CPMs) and, when applicable, normalized to input (ratio to matched input sample). For ENCODE samples, the fold change to input was similarly computed at 10 kb resolution from preprocessed BigWig files (Table S4) using deepTools (version 3.1.3, Ramirez et al., 2016). All genome-wide signals were then $\log_2$ transformed and cross-sample normalized by z-transformation, either relative to the mean signal and standard deviation per chromosome (representative profiles at selected regions and all genome-wide analyses) or across the set of centered locations for all heat maps. The only exceptions are replication timing (computed as the BrdU ratio in a given S phase fraction, relative to the maximum across all fractions, as described in Dellino et at. 2013), replication fork directionality (computed as the sum-difference ratio between Okazaki fragments mapped to the Crick and Watson strand, as described in Petryk et al., 2016) and the H3.3 to H3.1 ratio (computed as the sum-difference ratio between H3.3 and H3.1 per bin of 10 kb, ranging from -1 i.e. H3.1-only to +1 i.e. H3.3-only). All analyses were carried out with custom Python scripts using pandas (version 0.24.2, McKinney, 2010), NumPy (version 1.16.2, Harris et al., 2020) and SciPy (version 1.3.1, Virtanen et al., 2020). Plots were also generated with custom Python scripts using Matplotlib (version 2.2.4, Hunter, 2007) and seaborn (version 0.9.0, Waskom, 2021).

Chromatin segmentation and detection of H3.3-specific sites

We detected H3.3-specific sites based on H3.3/H3.1 patterns in G1/S cells, using a three-states Hidden Markov Model (HMM) to discriminate between H3.3- and H3.1-specific regions, or intervening sites where no variant is clearly prevalent or enriched relative to input. We inferred hidden states from a sequence of binary emissions measuring, per chromosome, the prevalence of H3.3-rich over H3.1-rich bins of 1 kb over a window of 10 consecutive bins (i.e. 1 kb bins where H3.3 or H3.1 showed higher CPMs than their respective input). Each chromosome was thus divided in 10 kb windows with a 0/1 emission: 1 if the number of H3.3-rich bins is greater than the number of H3.1-rich bins, 0 if the number is equal or lower. HMM emission probabilities were respectively initialized to 0.9 and 0.1 (for the H3.3-specific state), 0.5 and 0.5 (intermediate state), 0.1 and 0.9 (H3.1-specific state). The probability to remain in a given state was assumed to be the highest and initialized to 0.9, the transition probability to the intermediate state to 0.095, while direct transitions from H3.3- to H3.1-specific states (or vice versa) were assumed to be more unlikely and initialized to 0.005 probability. The transition probabilities from the intermediate to the H3.3- and H3.1-only states were instead assumed to be equal, and initialized to 0.05. The hidden state sequence was inferred after fitting the specified HMM on the observed emissions per chromosome based on the G1/S distribution in the parental H3.3-SNAP-HA and H3.1-SNAP-HA cell lines, with a convergence threshold of 0.01 and a maximum of 1000 EM algorithm iterations. The HMM scheme and estimated transition and emission

probabilities are illustrated in Figure S3A. H3.3 sites were defined from the sequence of hidden states, considering all continuous segments that were predicted as H3.3-specific and comprising a significant number of H3.3- or EdU-rich bins. For each site, we applied a one-tailed binomial test to assess if the number of enriched bins of 1 kb (i.e. with CPMs higher than corresponding input) was greater than expected by chance. We controlled the false discovery rate (FDR) via the Benjamini and Hochberg procedure, and only included sites where FDR < 10%. H3.3 sites showing a significant enrichment at 10% FDR were then ranked by nascent RNA content (mean counts per million from start to end position, pooled across replicates from Liang et al., 2015) and divided at the 5^{th} percentile into RNA^+ (top 95%) and RNA^- (bottom 5%). When comparing $HIRA^{WT}$ and $HIRA^{KO}$ cell lines, a two-tailed test was applied in $HIRA^{KO}$ cells to test whether the number of EdU-rich bins was significantly higher or lower than expected by chance. H3.3 sites showing a significant EdU enrichment in both $HIRA^{WT}$ and $HIRA^{KO}$ cells, after Benjamini-Hochberg correction, were classified as EdU^+ or "blurred sites". H3.3 sites enriched in $HIRA^{WT}$ cells but depleted in $HIRA^{KO}$ cells were classified as EdU^- or "buried sites". Analyses were carried out with custom Python scripts using pandas (version 0.24.2, McKinney, 2010), NumPy (version 1.16.2, Harris et al., 2020) and SciPy (version 1.3.1, Virtanen et al., 2020), HMMLearn (version 0.2.1) and statsmodels (version 0.10.1, Seabold et al., 2010) for HMM segmentation, domain detection, hypothesis testing and Benjamini-Hochberg correction. Matplotlib (version 2.2.4, Hunter, 2007), and seaborn (version 0.9.0, Waskom, 2021) were used for plotting.

Detection and classification of initiation zones based on H3.3 enrichment

Replication initiation zones (IZ) were inferred from OK-Seq data using a two-states HMM to identify the locations where the replication fork directionality (RFD) switches from negative (leftward-moving forks) to positive (rightward-moving forks). For each EdC replicate from Petryk et al., 2016, we converted the RFD signal to a series of binary emissions measuring, per chromosome, the directionality of the fork (1 if the RFD is positive, 0 otherwise) in non-overlapping windows of 10 kb. HMM emission probabilities were respectively initialized to 0.95 and 0.05 (rightward-moving state) and 0.05 and 0.95 (leftward-moving state). HMM transition probabilities were initialized to 0.95, for self-transitions, and 0.05, for transitions from the leftward- to the rightward-moving (and vice versa). The hidden state sequence was inferred after fitting the HMM on the sequence of binary emissions per chromosome, for each EdC replicate. Putative IZ locations were defined separately for both replicates, considering all genomic bins where the predicted state switched from 0 (leftward-moving) to 1 (rightward-moving). The ΔRFD was then computed at all locations as described in Petryk et al., 2016, after averaging the RFD signal over the two replicates. All IZ with a mean ΔRFD > 0 were included, except for IZ at consecutive locations (i.e. adjacent bins of 10 kb) where only the one with the highest ΔRFD was selected. IZ were then classified into H3.3-rich ($H3.3^+$) or H3.3-poor ($H3.3^-$) based on enrichment in G1/S cells (Table S3). The mean $\log_2$ ratio to input was computed at each IZ location ± 50 kb. IZ with a positive $\log_2$ ratio were classified as $H3.3^+$ (n = 5596), IZ with a negative $\log_2$ ratio were classified as $H3.3^-$ (n = 2417). In all heat maps, $H3.3^+$ and $H3.3^-$ IZ are sorted by ΔRFD and signals are visualized at bins of 1 kb around each location ± 0.2 Mb. Analyses were carried out with custom Python

scripts using pandas (version 0.24.2, McKinney, 2010), NumPy (version 1.16.2, Harris et al., 2020) and SciPy (version 1.3.1, Virtanen et al., 2020) and HMMLearn (version 0.2.1). Matplotlib (version 2.2.4, Hunter, 2007), and seaborn (version 0.9.0, Waskom, 2021) were used for plotting.

DNA combing

We measured fork speed in $HIRA^{WT}$ and $HIRA^{KO}$ H3.3-SNAP-HA cells by Replication Combing Assays (RCAs) (Bianco et al., 2020), using either asynchronous cells or G1/S synchronized cells, 1 hour after release into S phase. $HIRA^{WT}$ and $HIRA^{KO}$ cells were prepared in duplicates for RCA by two successive 30 minute pulses of CldU and IdU, and embedded in agarose. Combing, image acquisition and analysis was performed by Genomic Vision (http://www.genomicvision.com). We used only intact DNA fibers validated by DNA staining to calculate replication speed from the average CldU and IdU track length in kilobases per minute.

QUANTIFICATION AND STATISTICAL ANALYSIS

p-values were calculated by two-tailed Mann–Whitney U test (differences in proportions between $HIRA^{WT}$ and $HIRA^{KO}$ cells, Figure 6B and 6C) and two-tailed Welch's t-test (differences in fork speed, Figure 6D). Details are provided in Table S1, including adjusted p-values via Bonferroni correction for multiple testing. Differences with a p-value < 0.05 after Bonferroni correction were deemed as statistically significant.

References

Adam, S., Polo, S.E., Almouzni, G., 2013. Transcription Recovery after DNA Damage Requires Chromatin Priming by the H3.3 Histone Chaperone HIRA. Cell 155, 94–106. https://doi.org/10.1016/j.cell.2013.08.029

Almouzni, G., Cedar, H., 2016. Maintenance of Epigenetic Information. Cold Spring Harb Perspect Biol 8, a019372. https://doi.org/10.1101/cshperspect.a019372

Besnard, E., Babled, A., Lapasset, L., Milhavet, O., Parrinello, H., Dantec, C., Marin, J.-M., Lemaitre, J.-M., 2012. Unraveling cell type–specific and reprogrammable human replication origin signatures associated with G-quadruplex consensus motifs. Nat Struct Mol Biol 19, 837–844. https://doi.org/10.1038/nsmb.2339

Bianco, J.N., Poli, J., Saksouk, J., Bacal, J., Silva, M.J., Yoshida, K., Lin, Y.-L., Tourrière, H., Lengronne, A., Pasero, P., 2012. Analysis of DNA replication profiles in budding yeast and mammalian cells using DNA combing. Methods, DNA Replication Methods 57, 149–157. https://doi.org/10.1016/j.ymeth.2012.04.007

Buschbeck, M., Hake, S.B., 2017. Variants of core histones and their roles in cell fate decisions, development and cancer. Nat Rev Mol Cell Biol 18, 299–314. https://doi.org/10.1038/nrm.2016.166

Cayrou, C., Ballester, B., Peiffer, I., Fenouil, R., Coulombe, P., Andrau, J.-C., van Helden, J., Méchali, M., 2015. The chromatin environment shapes DNA replication origin organization and defines origin classes. Genome Res 25, 1873–1885. https://doi.org/10.1101/gr.192799.115

Cheloufi, S., Elling, U., Hopfgartner, B., Jung, Y.L., Murn, J., Ninova, M., Hubmann, M., Badeaux, A.I., Euong Ang, C., Tenen, D., Wesche, D.J., Abazova, N., Hogue, M., Tasdemir, N., Brumbaugh, J., Rathert, P., Jude, J., Ferrari, F., Blanco, A., Fellner, M., Wenzel, D., Zinner, M., Vidal, S.E., Bell, O., Stadtfeld, M., Chang, H.Y., Almouzni, G., Lowe, S.W., Rinn, J., Wernig, M., Aravin, A., Shi, Y., Park, P.J., Penninger, J.M., Zuber, J., Hochedlinger, K., 2015. The histone chaperone CAF-1 safeguards somatic cell identity. Nature 528, 218–224. https://doi.org/10.1038/nature15749

Chen, Y.-H., Keegan, S., Kahli, M., Tonzi, P., Fenyö, D., Huang, T.T., Smith, D.J., 2019. Transcription shapes DNA replication initiation and termination in human cells. Nat Struct Mol Biol 26, 67–77. https://doi.org/10.1038/s41594-018-0171-0

Clément, C., Orsi, G.A., Gatto, A., Boyarchuk, E., Forest, A., Hajj, B., Miné-Hattab, J., Garnier, M., Gurard-Levin, Z.A., Quivy, J.-P., Almouzni, G., 2018. High-resolution visualization of H3 variants during replication reveals their controlled recycling. Nat Commun 9, 3181. https://doi.org/10.1038/s41467-018-05697-1

Danecek, P., Bonfield, J.K., Liddle, J., Marshall, J., Ohan, V., Pollard, M.O., Whitwham, A., Keane, T., McCarthy, S.A., Davies, R.M., Li, H., 2021. Twelve years of SAMtools and BCFtools. Gigascience 10, giab008. https://doi.org/10.1093/gigascience/giab008

Davis, C.A., Hitz, B.C., Sloan, C.A., Chan, E.T., Davidson, J.M., Gabdank, I., Hilton, J.A., Jain, K., Baymuradov, U.K., Narayanan, A.K., Onate, K.C., Graham, K., Miyasato, S.R., Dreszer, T.R., Strattan, J.S., Jolanki, O., Tanaka, F.Y., Cherry, J.M., 2018. The Encyclopedia of DNA elements (ENCODE): data portal update. Nucleic Acids Res 46, D794–D801. https://doi.org/10.1093/nar/gkx1081

Deal, R.B., Henikoff, J.G., Henikoff, S., 2010. Genome-Wide Kinetics of Nucleosome Turnover Determined by Metabolic Labeling of Histones. Science 328, 1161–1164. https://doi.org/10.1126/science.1186777

Dellino, G.I., Cittaro, D., Piccioni, R., Luzi, L., Banfi, S., Segalla, S., Cesaroni, M., Mendoza-Maldonado, R., Giacca, M., Pelicci, P.G., 2013. Genome-wide mapping of human DNA-replication origins: Levels of transcription at ORC1 sites regulate origin selection and replication timing. Genome Res. 23, 1–11. https://doi.org/10.1101/gr.142331.112

DePamphilis, M.L., 2016. Chapter Two - Genome Duplication at the Beginning of Mammalian Development, in: DePamphilis, Melvin L. (Ed.), Current Topics in Developmental Biology, Mammalian Preimplantation Development. Academic Press, pp. 55–102. https://doi.org/10.1016/bs.ctdb.2016.04.003

DePamphilis, M.L., 1988. Transcriptional elements as components of eukaryotic origins of DNA replication. Cell 52, 635–638. https://doi.org/10.1016/0092-8674(88)90398-4

Escobar, T.M., Oksuz, O., Saldaña-Meyer, R., Descostes, N., Bonasio, R., Reinberg, D., 2019. Active and Repressed Chromatin Domains Exhibit Distinct Nucleosome Segregation during DNA Replication. Cell 179, 953-963.e11. https://doi.org/10.1016/j.cell.2019.10.009

Fragkos, M., Ganier, O., Coulombe, P., Méchali, M., 2015. DNA replication origin activation in space and time. Nat Rev Mol Cell Biol 16, 360–374. https://doi.org/10.1038/nrm4002

Goldberg, A.D., Banaszynski, L.A., Noh, K.-M., Lewis, P.W., Elsaesser, S.J., Stadler, S., Dewell, S., Law, M., Guo, X., Li, X., Wen, D., Chapgier, A., DeKelver, R.C., Miller, J.C., Lee, Y.-L., Boydston, E.A., Holmes, M.C., Gregory, P.D., Greally, J.M., Rafii, S., Yang, C., Scambler, P.J., Garrick, D., Gibbons, R.J., Higgs, D.R., Cristea, I.M., Urnov, F.D., Zheng, D., Allis, C.D., 2010. Distinct Factors Control Histone Variant H3.3 Localization at Specific Genomic Regions. Cell 140, 678–691. https://doi.org/10.1016/j.cell.2010.01.003

Gomes, A.P., Ilter, D., Low, V., Rosenzweig, A., Shen, Z.-J., Schild, T., Rivas, M.A., Er, E.E., McNally, D.R., Mutvei, A.P., Han, J., Ou, Y.-H., Cavaliere, P., Mullarky, E., Nagiec, M., Shin, S., Yoon, S.-O., Dephoure, N., Massagué, J., Melnick, A.M., Cantley, L.C., Tyler, J.K., Blenis, J., 2019. Dynamic Incorporation of Histone H3 Variants into Chromatin Is Essential for Acquisition of Aggressive Traits and Metastatic Colonization. Cancer Cell 36, 402-417.e13. https://doi.org/10.1016/j.ccell.2019.08.006

Hansen, R.S., Thomas, S., Sandstrom, R., Canfield, T.K., Thurman, R.E., Weaver, M., Dorschner, M.O., Gartler, S.M., Stamatoyannopoulos, J.A., 2010. Sequencing newly replicated DNA reveals widespread plasticity in human replication timing. PNAS 107, 139–144. https://doi.org/10.1073/pnas.0912402107

Harris, C.R., Millman, K.J., van der Walt, S.J., Gommers, R., Virtanen, P., Cournapeau, D., Wieser, E., Taylor, J., Berg, S., Smith, N.J., Kern, R., Picus, M., Hoyer, S., van Kerkwijk, M.H., Brett, M., Haldane, A., del Río, J.F., Wiebe, M., Peterson, P., Gérard-Marchant, P., Sheppard, K., Reddy, T., Weckesser, W., Abbasi, H., Gohlke, C., Oliphant, T.E., 2020. Array programming with NumPy. Nature 585, 357–362. https://doi.org/10.1038/s41586-020-2649-2

Hiratani, I., Ryba, T., Itoh, M., Yokochi, T., Schwaiger, M., Chang, C.-W., Lyou, Y., Townes, T.M., Schübeler, D., Gilbert, D.M., 2008. Global Reorganization of Replication Domains During Embryonic Stem Cell Differentiation. PLOS Biology 6, e245. https://doi.org/10.1371/journal.pbio.0060245

Hiratani, I., Ryba, T., Itoh, M., Rathjen, J., Kulik, M., Papp, B., Fussner, E., Bazett-Jones, D.P., Plath, K., Dalton, S., Rathjen, P.D., Gilbert, D.M., 2010. Genome-wide dynamics of replication timing revealed by in vitro models of mouse embryogenesis. Genome Res. 20, 155–169. https://doi.org/10.1101/gr.099796.109

Hörmanseder, E., Simeone, A., Allen, G.E., Bradshaw, C.R., Figlmüller, M., Gurdon, J., Jullien, J., 2017. H3K4 Methylation-Dependent Memory of Somatic Cell Identity Inhibits Reprogramming and Development of Nuclear Transfer Embryos. Cell Stem Cell 21, 135-143.e6. https://doi.org/10.1016/j.stem.2017.03.003

Hunter, J.D., 2007. Matplotlib: A 2D Graphics Environment. Computing in Science Engineering 9, 90–95. https://doi.org/10.1109/MCSE.2007.55

Hyrien, O., Maric, C., Méchali, M., 1995. Transition in Specification of Embryonic Metazoan DNA Replication Origins. Science 270, 994–997. https://doi.org/10.1126/science.270.5238.994

Hyrien, O., Méchali, M., 1993. Chromosomal replication initiates and terminates at random sequences but at regular intervals in the ribosomal DNA of Xenopus early embryos. EMBO J 12, 4511–4520. https://doi.org/10.1002/j.1460-2075.1993.tb06140.x

Kim, D., Paggi, J.M., Park, C., Bennett, C., Salzberg, S.L., 2019. Graph-based genome alignment and genotyping with HISAT2 and HISAT-genotype. Nat Biotechnol 37, 907–915. https://doi.org/10.1038/s41587-019-0201-4

Klein, K.N., Zhao, P.A., Lyu, X., Sasaki, T., Bartlett, D.A., Singh, A.M., Tasan, I., Zhang, M., Watts, L.P., Hiraga, S., Natsume, T., Zhou, X., Baslan, T., Leung, D., Kanemaki, M.T., Donaldson, A.D., Zhao, H., Dalton, S., Corces, V.G., Gilbert, D.M., 2021a. Replication timing maintains the global epigenetic state in human cells. Science 372, 371–378. https://doi.org/10.1126/science.aba5545

Langmead, B., Salzberg, S.L., 2012. Fast gapped-read alignment with Bowtie 2. Nat Methods 9, 357–359. https://doi.org/10.1038/nmeth.1923

Liang, K., Woodfin, A.R., Slaughter, B.D., Unruh, J.R., Box, A.C., Rickels, R.A., Gao, X., Haug, J.S., Jaspersen, S.L., Shilatifard, A., 2015. Mitotic Transcriptional Activation: Clearance of Actively Engaged Pol II Via Transcriptional Elongation Control in Mitosis. Mol Cell 60, 435–445. https://doi.org/10.1016/j.molcel.2015.09.021

Lin, C.-J., Koh, F.M., Wong, P., Conti, M., Ramalho-Santos, M., 2014. Hira-mediated H3.3 incorporation is required for DNA replication and ribosomal RNA transcription in the mouse zygote. Dev Cell 30, 268–279. https://doi.org/10.1016/j.devcel.2014.06.022

Lin, Y.-L., Pasero, P., 2012. Interference Between DNA Replication and Transcription as a Cause of Genomic Instability. Current Genomics 13, 65–73. https://doi.org/10.2174/138920212799034767

Long, H., Zhang, L., Lv, M., Wen, Z., Zhang, W., Chen, X., Zhang, P., Li, T., Chang, L., Jin, C., Wu, G., Wang, X., Yang, F., Pei, J., Chen, P., Margueron, R., Deng, H., Zhu, M., Li, G., 2020. H2A.Z facilitates licensing and activation of early replication origins. Nature 577, 576–581. https://doi.org/10.1038/s41586-019-1877-9

Macheret, M., Halazonetis, T.D., 2018. Intragenic origins due to short G1 phases underlie oncogene-induced DNA replication stress. Nature 555, 112–116. https://doi.org/10.1038/nature25507

Marchal, C., Sima, J., Gilbert, D.M., 2019. Control of DNA replication timing in the 3D genome. Nat Rev Mol Cell Biol 20, 721–737. https://doi.org/10.1038/s41580-019-0162-y

Martire, S., Banaszynski, L.A., 2020. The roles of histone variants in fine-tuning chromatin organization and function. Nat Rev Mol Cell Biol 21, 522–541. https://doi.org/10.1038/s41580-020-0262-8

Martire, S., Gogate, A.A., Whitmill, A., Tafessu, A., Nguyen, J., Teng, Y.-C., Tastemel, M., Banaszynski, L.A., 2019. Phosphorylation of histone H3.3 at serine 31 promotes p300 activity and enhancer acetylation. Nat Genet 51, 941–946. https://doi.org/10.1038/s41588-019-0428-5

McKinney, W., 2010. Data Structures for Statistical Computing in Python, in: Walt, S. van der, Millman, J. (Eds.), Proceedings of the 9th Python in Science Conference. pp. 56–61. https://doi.org/10.25080/Majora-92bf1922-00a

Miotto, B., Ji, Z., Struhl, K., 2016. Selectivity of ORC binding sites and the relation to replication timing, fragile sites, and deletions in cancers. PNAS 113, E4810–E4819. https://doi.org/10.1073/pnas.1609060113

Nacev, B.A., Feng, L., Bagert, J.D., Lemiesz, A.E., Gao, J., Soshnev, A.A., Kundra, R., Schultz, N., Muir, T.W., Allis, C.D., 2019. The expanding landscape of 'oncohistone' mutations in human cancers. Nature 567, 473–478. https://doi.org/10.1038/s41586-019-1038-1

Ng, R.K., Gurdon, J.B., 2008. Epigenetic memory of an active gene state depends on histone H3.3 incorporation into chromatin in the absence of transcription. Nat Cell Biol 10, 102–109. https://doi.org/10.1038/ncb1674

Paranjape, N.P., Calvi, B.R., 2016. The Histone Variant H3.3 Is Enriched at Drosophila Amplicon Origins but Does Not Mark Them for Activation. G3 (Bethesda) 6, 1661–1671. https://doi.org/10.1534/g3.116.028068

Pelham-Webb, B., Polyzos, A., Wojenski, L., Kloetgen, A., Li, J., Di Giammartino, D.C., Sakellaropoulos, T., Tsirigos, A., Core, L., Apostolou, E., 2021. H3K27ac bookmarking promotes rapid post-mitotic activation of the pluripotent stem cell program without impacting 3D chromatin reorganization. Mol Cell 81, 1732-1748.e8. https://doi.org/10.1016/j.molcel.2021.02.032

Petryk, N., Kahli, M., d'Aubenton-Carafa, Y., Jaszczyszyn, Y., Shen, Y., Silvain, M., Thermes, C., Chen, C.-L., Hyrien, O., 2016. Replication landscape of the human genome. Nat Commun 7, 10208. https://doi.org/10.1038/ncomms10208

Prioleau, M.-N., MacAlpine, D.M., 2016. DNA replication origins—where do we begin? Genes Dev. 30, 1683–1697. https://doi.org/10.1101/gad.285114.116

Probst, A.V., Dunleavy, E., Almouzni, G., 2009. Epigenetic inheritance during the cell cycle. Nat Rev Mol Cell Biol 10, 192–206. https://doi.org/10.1038/nrm2640

Promonet, A., Padioleau, I., Liu, Y., Sanz, L., Biernacka, A., Schmitz, A.-L., Skrzypczak, M., Sarrazin, A., Mettling, C., Rowicka, M., Ginalski, K., Chedin, F., Chen, C.-L., Lin, Y.-L., Pasero, P., 2020. Topoisomerase 1 prevents replication stress at R-loop-enriched transcription termination sites. Nat Commun 11, 3940. https://doi.org/10.1038/s41467-020-17858-2

Quinlan, A.R., Hall, I.M., 2010. BEDTools: a flexible suite of utilities for comparing genomic features. Bioinformatics 26, 841–842. https://doi.org/10.1093/bioinformatics/btq033

Ramírez, F., Ryan, D.P., Grüning, B., Bhardwaj, V., Kilpert, F., Richter, A.S., Heyne, S., Dündar, F., Manke, T., 2016. deepTools2: a next generation web server for deep-sequencing data analysis. Nucleic Acids Res 44, W160-165. https://doi.org/10.1093/nar/gkw257

Rausch, C., Weber, P., Prorok, P., Hörl, D., Maiser, A., Lehmkuhl, A., Chagin, V.O., Casas-Delucchi, C.S., Leonhardt, H., Cardoso, M.C., 2020. Developmental differences in genome replication program and origin activation. Nucleic Acids Research 48, 12751–12777. https://doi.org/10.1093/nar/gkaa1124

Ray-Gallet, D., Almouzni, G., 2021. The Histone H3 Family and Its Deposition Pathways, in: Fang, D., Han, J. (Eds.), Histone Mutations and Cancer, Advances in Experimental Medicine and Biology. Springer, Singapore, pp. 17–42. https://doi.org/10.1007/978-981-15-8104-5_2

Ray-Gallet, D., Almouzni, G., 2010. Mixing or Not Mixing. Science 328, 56–57. https://doi.org/10.1126/science.1188653

Ray-Gallet, D., Ricketts, M.D., Sato, Y., Gupta, K., Boyarchuk, E., Senda, T., Marmorstein, R., Almouzni, G., 2018. Functional activity of the H3.3 histone chaperone complex HIRA requires trimerization of the HIRA subunit. Nat Commun 9, 3103. https://doi.org/10.1038/s41467-018-05581-y

Ray-Gallet, D., Woolfe, A., Vassias, I., Pellentz, C., Lacoste, N., Puri, A., Schultz, D.C., Pchelintsev, N.A., Adams, P.D., Jansen, L.E.T., Almouzni, G., 2011. Dynamics of Histone H3 Deposition In Vivo Reveal a Nucleosome Gap-Filling Mechanism for H3.3 to Maintain Chromatin Integrity. Molecular Cell 44, 928–941. https://doi.org/10.1016/j.molcel.2011.12.006

Reinberg, D., Vales, L.D., 2018. Chromatin domains rich in inheritance. Science 361, 33–34. https://doi.org/10.1126/science.aat7871

Rivera-Mulia, J.C., Buckley, Q., Sasaki, T., Zimmerman, J., Didier, R.A., Nazor, K., Loring, J.F., Lian, Z., Weissman, S., Robins, A.J., Schulz, T.C., Menendez, L., Kulik, M.J., Dalton, S., Gabr, H., Kahveci, T., Gilbert, D.M., 2015. Dynamic changes in replication timing and gene expression during lineage specification of human pluripotent stem cells. Genome Res 25, 1091–1103. https://doi.org/10.1101/gr.187989.114

Romanoski, C.E., Glass, C.K., Stunnenberg, H.G., Wilson, L., Almouzni, G., 2015. Roadmap for regulation. Nature 518, 314–316. https://doi.org/10.1038/518314a

Sarthy JF, Meers MP, Janssens DH, Henikoff JG, Feldman H, Paddison PJ, Lockwood CM, Vitanza NA, Olson JM, Ahmad K, Henikoff S., 2020. Histone deposition pathways determine the chromatin landscapes of H3.1 and H3.3 K27M oncohistones. Elife. 9:e61090. https://doi.org/10.7554/eLife.61090

Sasaki, T., Sawado, T., Yamaguchi, M., Shinomiya, T., 1999. Specification of Regions of DNA Replication Initiation during Embryogenesis in the 65-Kilobase DNApolα-dE2F Locus of Drosophila melanogaster. Mol Cell Biol 19, 547–555. https://doi.org/10.1128/MCB.19.1.547

Seabold, S., Perktold, J., 2010. Statsmodels: Econometric and Statistical Modeling with Python. Presented at the Python in Science Conference, Austin, Texas, pp. 92–96. https://doi.org/10.25080/Majora-92bf1922-011

Shibahara, K., Stillman, B., 1999. Replication-Dependent Marking of DNA by PCNA Facilitates CAF-1-Coupled Inheritance of Chromatin. Cell 96, 575–585. https://doi.org/10.1016/S0092-8674(00)80661-3

Siefert, J.C., Georgescu, C., Wren, J.D., Koren, A., Sansam, C.L., 2017. DNA replication timing during development anticipates transcriptional programs and parallels enhancer activation. Genome Res. 27, 1406–1416. https://doi.org/10.1101/gr.218602.116

Sima, J., Chakraborty, A., Dileep, V., Michalski, M., Klein, K.N., Holcomb, N.P., Turner, J.L., Paulsen, M.T., Rivera-Mulia, J.C., Trevilla-Garcia, C., Bartlett, D.A., Zhao, P.A., Washburn, B.K., Nora, E.P., Kraft, K., Mundlos, S., Bruneau, B.G., Ljungman, M., Fraser, P., Ay, F., Gilbert, D.M., 2019. Identifying cis Elements for Spatiotemporal Control of Mammalian DNA Replication. Cell 176, 816-830.e18. https://doi.org/10.1016/j.cell.2018.11.036

Sitbon, D., Boyarchuk, E., Dingli, F., Loew, D., Almouzni, G., 2020. Histone variant H3.3 residue S31 is essential for Xenopus gastrulation regardless of the deposition pathway. Nat Commun 11, 1256. https://doi.org/10.1038/s41467-020-15084-4

Stewart-Morgan, K.R., Petryk, N., Groth, A., 2020. Chromatin replication and epigenetic cell memory. Nat Cell Biol 22, 361–371. https://doi.org/10.1038/s41556-020-0487-y

Strobino, M., Wenda, J.M., Padayachy, L., Steiner, F.A., 2020. Loss of histone H3.3 results in DNA replication defects and altered origin dynamics in C. elegans. Genome Res. https://doi.org/10.1101/gr.260794.120

Szenker, E., Boyarchuk, E., Almouzni, G., 2014. Properties and Functions of Histone Variants, in: Workman, J.L., Abmayr, S.M. (Eds.), Fundamentals of Chromatin. Springer, New York, NY, pp. 375–426. https://doi.org/10.1007/978-1-4614-8624-4_10

Taddei, A., Roche, D., Sibarita, J.B., Turner, B.M., Almouzni, G., 1999. Duplication and maintenance of heterochromatin domains. J Cell Biol 147, 1153–1166. https://doi.org/10.1083/jcb.147.6.1153

Tagami, H., Ray-Gallet, D., Almouzni, G., Nakatani, Y., 2004. Histone H3.1 and H3.3 Complexes Mediate Nucleosome Assembly Pathways Dependent or Independent of DNA Synthesis. Cell 116, 51–61. https://doi.org/10.1016/S0092-8674(03)01064-X

Torné, J., Ray-Gallet, D., Boyarchuk, E., Garnier, M., Le Baccon, P., Coulon, A., Orsi, G.A., Almouzni, G., 2020. Two HIRA-dependent pathways mediate H3.3 de novo deposition and recycling during transcription. Nat Struct Mol Biol 27, 1057–1068. https://doi.org/10.1038/s41594-020-0492-7

Vermeulen, M., Eberl, H.C., Matarese, F., Marks, H., Denissov, S., Butter, F., Lee, K.K., Olsen, J.V., Hyman, A.A., Stunnenberg, H.G., Mann, M., 2010. Quantitative interaction proteomics and genome-wide profiling of epigenetic histone marks and their readers. Cell 142, 967–980. https://doi.org/10.1016/j.cell.2010.08.020

Virtanen, P., Gommers, R., Oliphant, T.E., Haberland, M., Reddy, T., Cournapeau, D., Burovski, E., Peterson, P., Weckesser, W., Bright, J., van der Walt, S.J., Brett, M., Wilson, J., Millman, K.J., Mayorov, N., Nelson, A.R.J., Jones, E., Kern, R., Larson, E., Carey, C.J., Polat, İ., Feng, Y., Moore, E.W., VanderPlas, J., Laxalde, D., Perktold, J., Cimrman, R., Henriksen, I., Quintero, E.A., Harris, C.R., Archibald, A.M., Ribeiro, A.H., Pedregosa, F., van Mulbregt, P., 2020. SciPy 1.0: fundamental algorithms for scientific computing in Python. Nat Methods 17, 261–272. https://doi.org/10.1038/s41592-019-0686-2

Wang, W., Klein, K.N., Proesmans, K., Yang, H., Marchal, C., Zhu, X., Borrman, T., Hastie, A., Weng, Z., Bechhoefer, J., Chen, C.-L., Gilbert, D.M., Rhind, N., 2021. Genome-wide mapping of human DNA replication by optical replication mapping supports a stochastic model of eukaryotic replication. Molecular Cell. https://doi.org/10.1016/j.molcel.2021.05.024

Waskom, M.L., 2021. seaborn: statistical data visualization. Journal of Open Source Software 6, 3021. https://doi.org/10.21105/joss.03021

Waterborg, J.H., 2012. Evolution of histone H3: emergence of variants and conservation of post-translational modification sites1This article is part of Special Issue entitled Asilomar Chromatin and has undergone the Journal's usual peer review process. Biochem. Cell Biol. 90, 79–95. https://doi.org/10.1139/o11-036

Wu, R., Wang, Z., Zhang, H., Gan, H., Zhang, Z., 2017. H3K9me3 demethylase Kdm4d facilitates the formation of pre-initiative complex and regulates DNA replication. Nucleic Acids Res 45, 169–180. https://doi.org/10.1093/nar/gkw848

Yadav, T., Quivy, J.-P., Almouzni, G., 2018. Chromatin plasticity: A versatile landscape that underlies cell fate and identity. Science 361, 1332–1336. https://doi.org/10.1126/science.aat8950

Yekezare, M., Gómez-González, B., Diffley, J.F.X., 2013. Controlling DNA replication origins in response to DNA damage – inhibit globally, activate locally. Journal of Cell Science 126, 1297–1306. https://doi.org/10.1242/jcs.096701

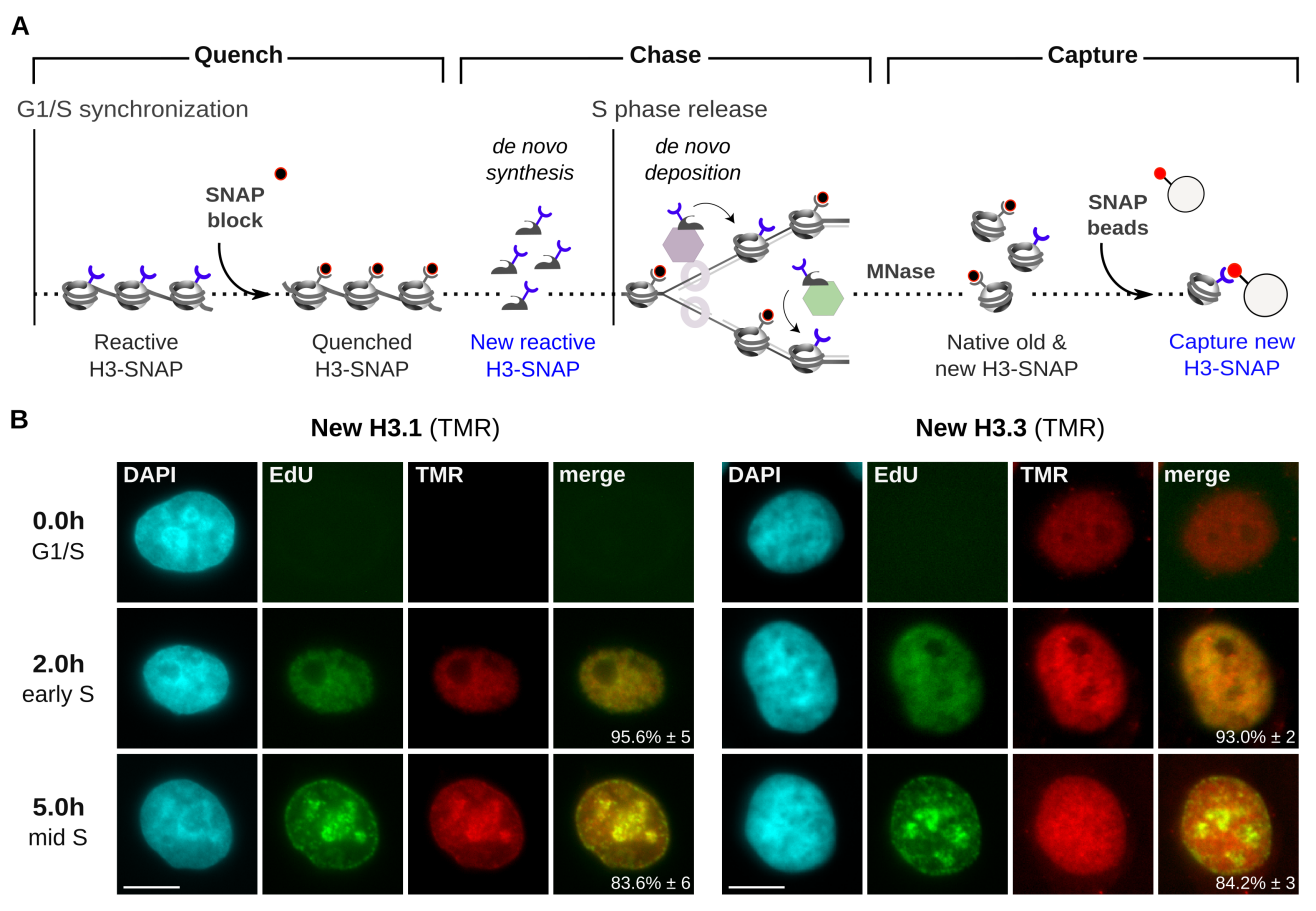
A
Quench
Chase
Capture
G1/S synchronization
S phase release
SNAP block
de novo synthesis
de novo deposition
MNase
SNAP beads
Reactive H3-SNAP
Quenched H3-SNAP
New reactive H3-SNAP
Native old & new H3-SNAP
Capture new H3-SNAP
B
New H3.1 (TMR)
New H3.3 (TMR)
DAPI
EdU
TMR
merge
0.0h G1/S
2.0h early S
5.0h mid S
95.6% ± 5
83.6% ± 6
93.0% ± 2
84.2% ± 3

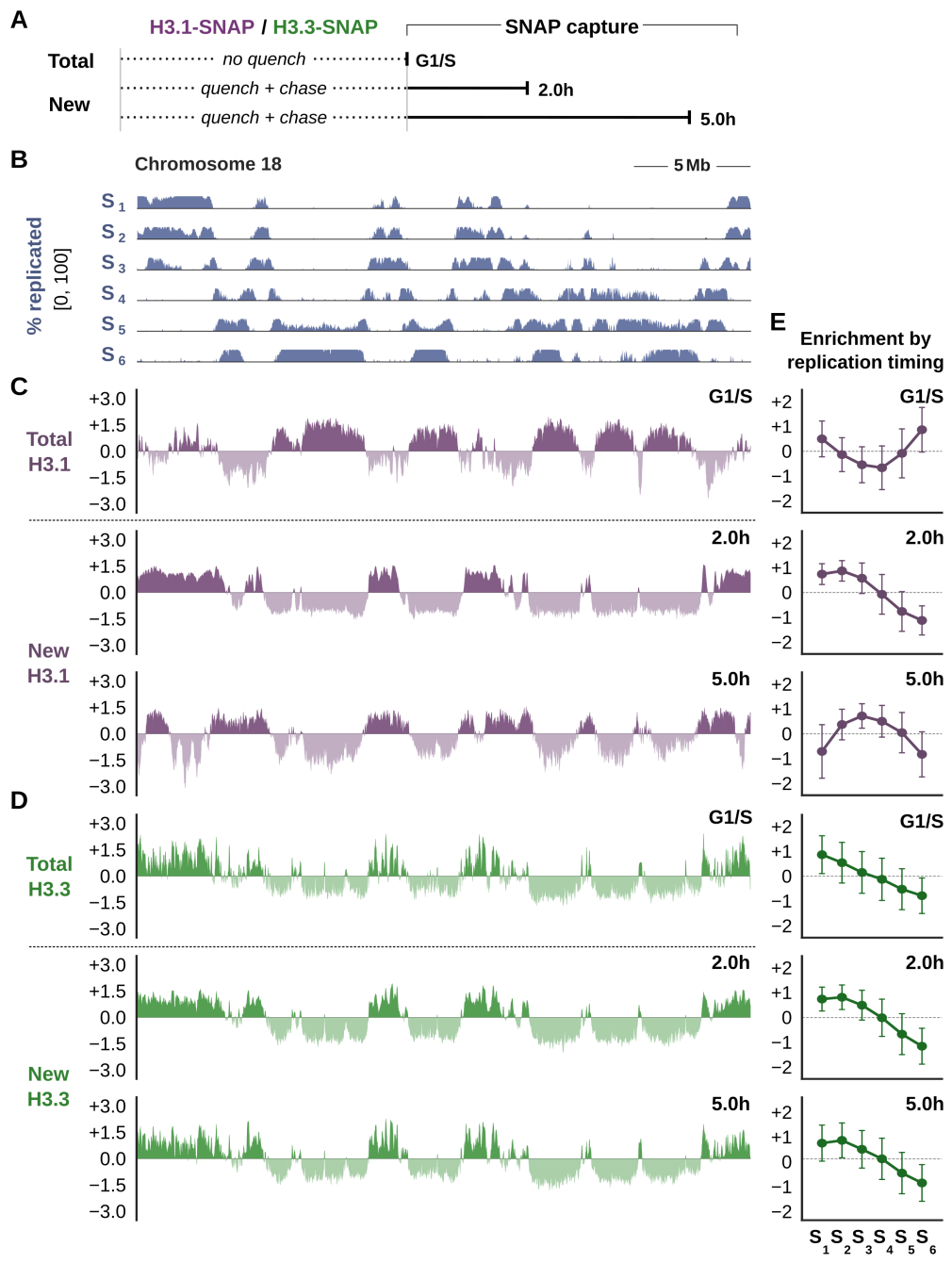
A
H3.1-SNAP / H3.3-SNAP
SNAP capture
Total
no quench
G1/S
New
quench + chase
2.0h
quench + chase
5.0h
B
Chromosome 18
5 Mb
% replicated
[0, 100]
S1
S2
S3
S4
S5
S6
C
Total H3.1
New H3.1
D
Total H3.3
New H3.3
G1/S
2.0h
5.0h
+3.0
+1.5
0.0
−1.5
−3.0
E
Enrichment by replication timing
+2
+1
0
−1
−2
S1 S2 S3 S4 S5 S6

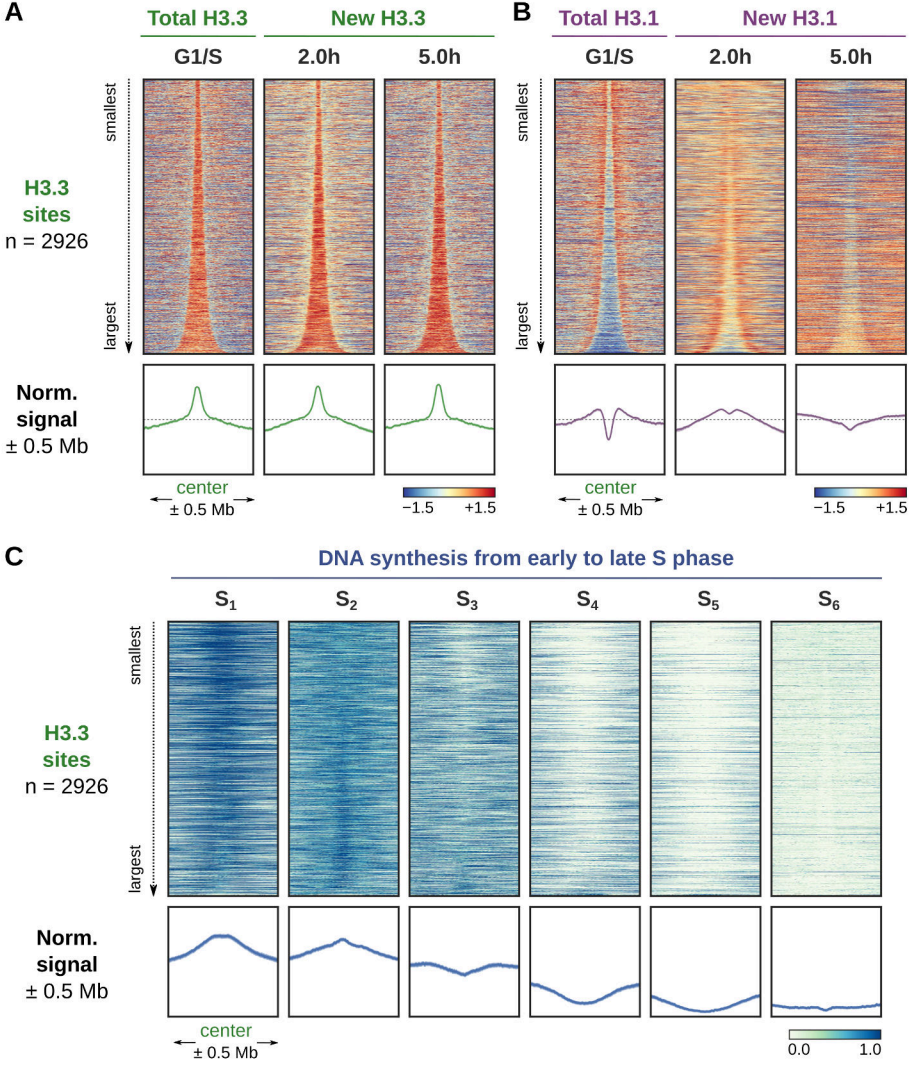
A
Total H3.3
New H3.3
G1/S
2.0h
5.0h
smallest
largest
H3.3 sites
n = 2926
Norm. signal
± 0.5 Mb
center
± 0.5 Mb
−1.5
+1.5
B
Total H3.1
New H3.1
G1/S
2.0h
5.0h
smallest
largest
center
± 0.5 Mb
−1.5
+1.5
C
DNA synthesis from early to late S phase
S1
S2
S3
S4
S5
S6
smallest
largest
H3.3 sites
n = 2926
Norm. signal
± 0.5 Mb
center
± 0.5 Mb
0.0
1.0

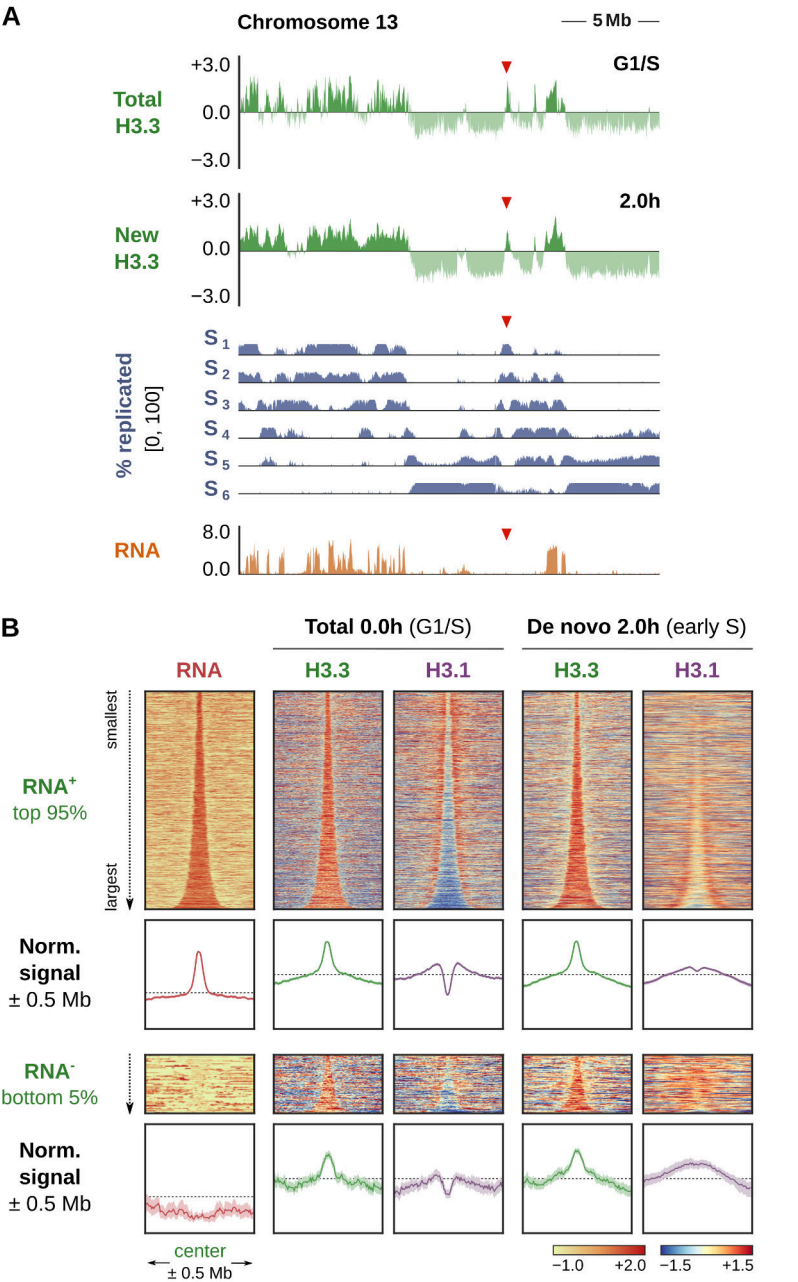
A
Chromosome 13
5 Mb
G1/S
Total H3.3
+3.0
0.0
−3.0
2.0h
New H3.3
% replicated
[0, 100]
S 1
S 2
S 3
S 4
S 5
S 6
RNA
8.0
0.0
B
Total 0.0h (G1/S)
De novo 2.0h (early S)
RNA
H3.3
H3.1
smallest
largest
RNA+
top 95%
Norm. signal
± 0.5 Mb
RNA-
bottom 5%
center
± 0.5 Mb
−1.0
+2.0
−1.5
+1.5

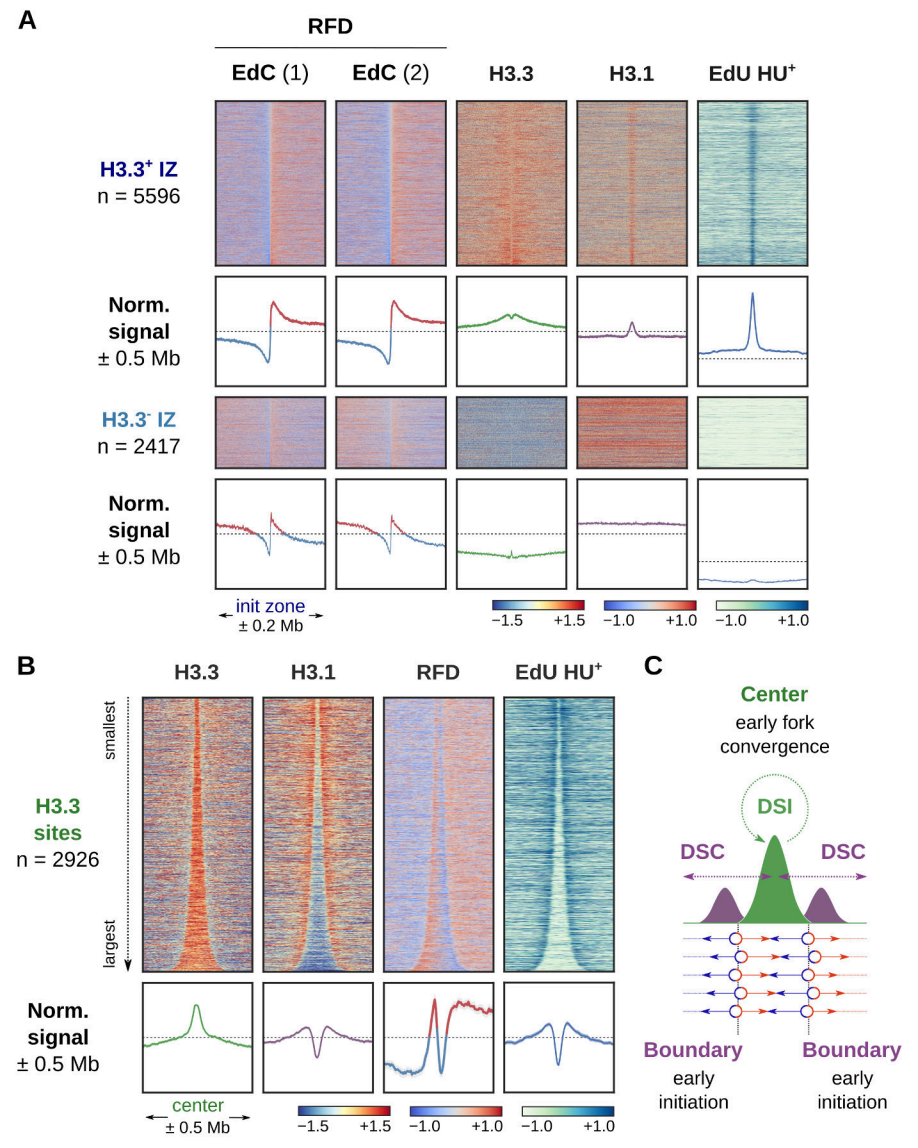
A
RFD
EdC (1)
EdC (2)
H3.3
H3.1
EdU HU+
H3.3+ IZ
n = 5596
Norm. signal
± 0.5 Mb
H3.3- IZ
n = 2417
Norm. signal
± 0.5 Mb
init zone
± 0.2 Mb
−1.5 +1.5
−1.0 +1.0
−1.0 +1.0
B
H3.3
H3.1
RFD
EdU HU+
smallest
largest
H3.3 sites
n = 2926
Norm. signal
± 0.5 Mb
center
± 0.5 Mb
−1.5 +1.5
−1.0 +1.0
−1.0 +1.0
C
Center
early fork convergence
DSI
DSC
DSC
Boundary
early initiation
Boundary
early initiation

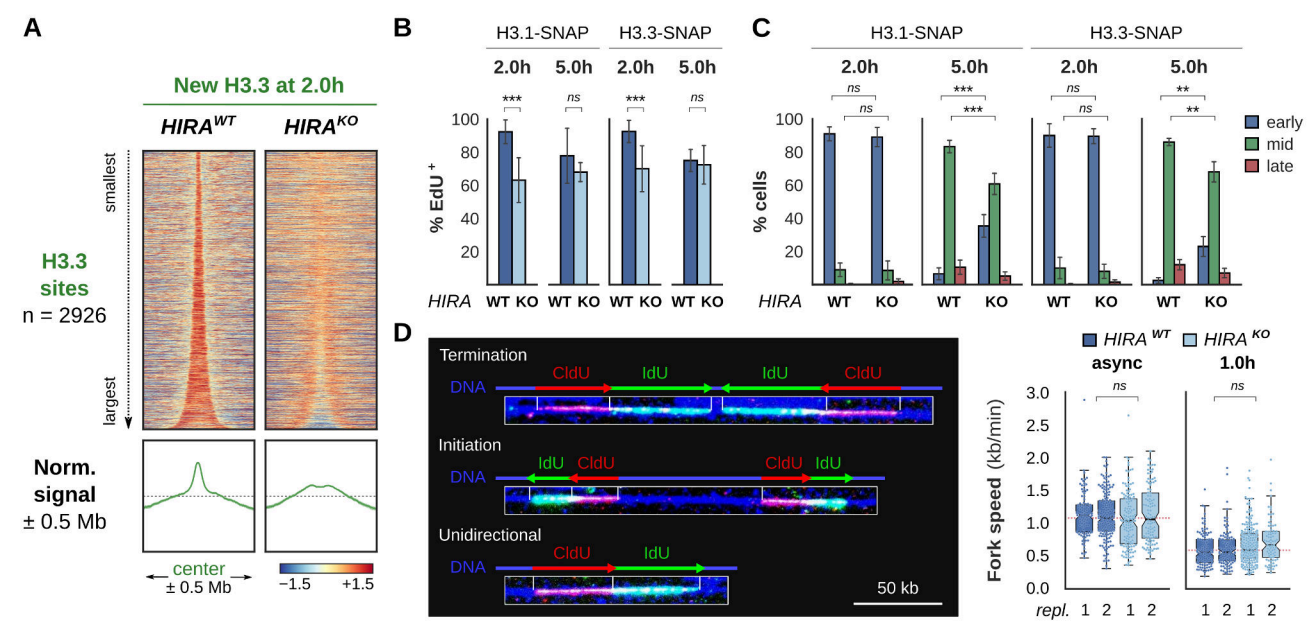
A
New H3.3 at 2.0h
HIRA^WT
HIRA^KO
smallest
largest
H3.3 sites
n = 2926
Norm. signal
± 0.5 Mb
center
± 0.5 Mb
−1.5
+1.5
B
H3.1-SNAP
H3.3-SNAP
2.0h
5.0h
2.0h
5.0h
% EdU +
***
ns
***
ns
HIRA
WT KO WT KO WT KO WT KO
C
H3.1-SNAP
H3.3-SNAP
2.0h
5.0h
2.0h
5.0h
% cells
ns
ns
***
***
ns
ns
**
**
early
mid
late
HIRA
WT
KO
WT
KO
WT
KO
WT
KO
D
Termination
DNA
CldU
IdU
IdU
CldU
Initiation
DNA
IdU
CldU
CldU
IdU
Unidirectional
DNA
CldU
IdU
50 kb
HIRA WT
HIRA KO
async
1.0h
Fork speed (kb/min)
ns
ns
repl.
1 2 1 2
1 2 1 2

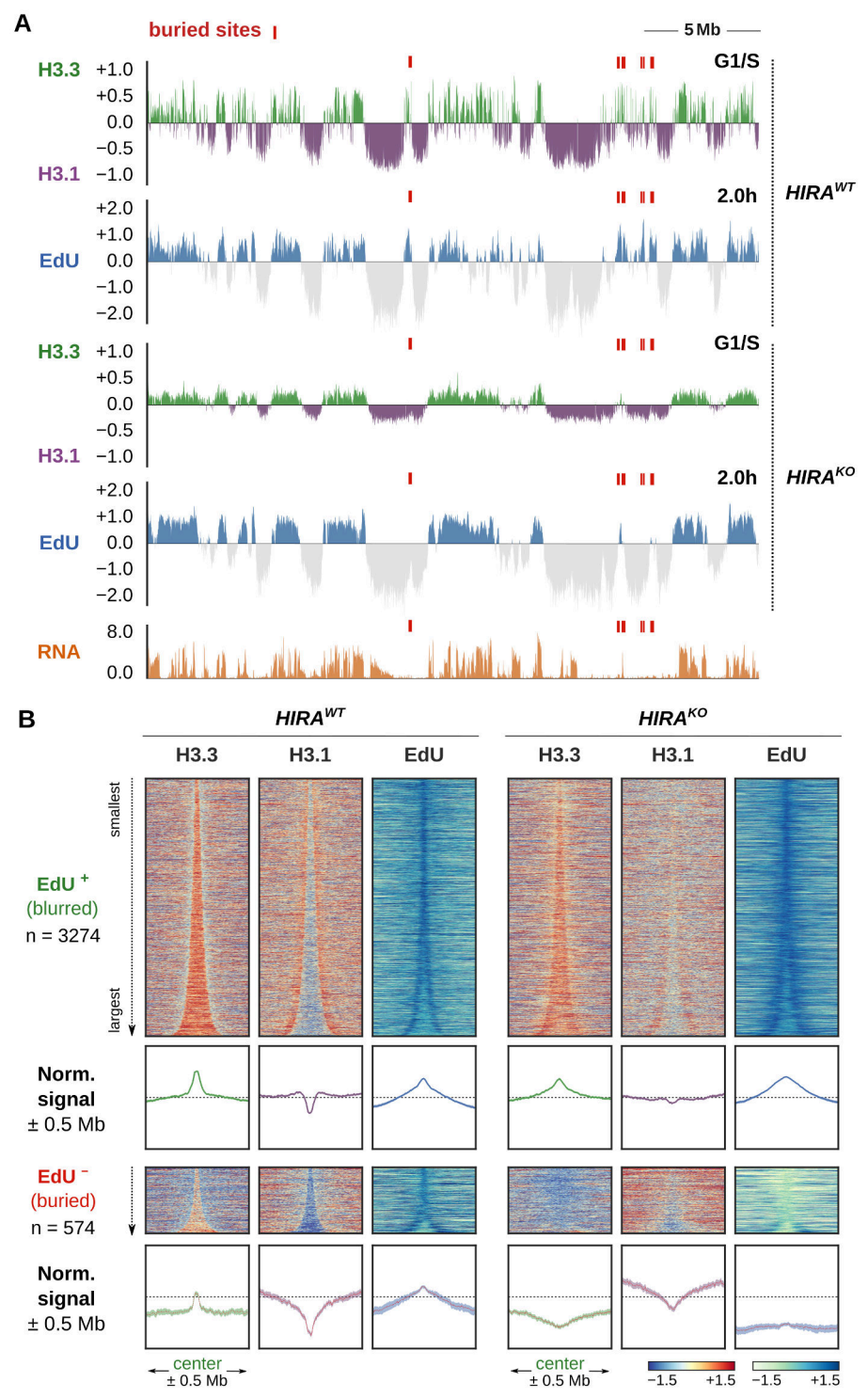
A
buried sites
5 Mb
H3.3
H3.1
EdU
RNA
G1/S
2.0h
HIRA^WT
HIRA^KO
+1.0
+0.5
0.0
−0.5
−1.0
+2.0
−2.0
8.0
B
HIRA^WT
HIRA^KO
H3.3
H3.1
EdU
smallest
largest
EdU + (blurred)
n = 3274
EdU − (buried)
n = 574
Norm. signal
± 0.5 Mb
center
± 0.5 Mb
−1.5
+1.5

HIRA WT

HIRA KO

deposition

occupancy

H3.1

H3.3

transcription

transcription + **HIRA**

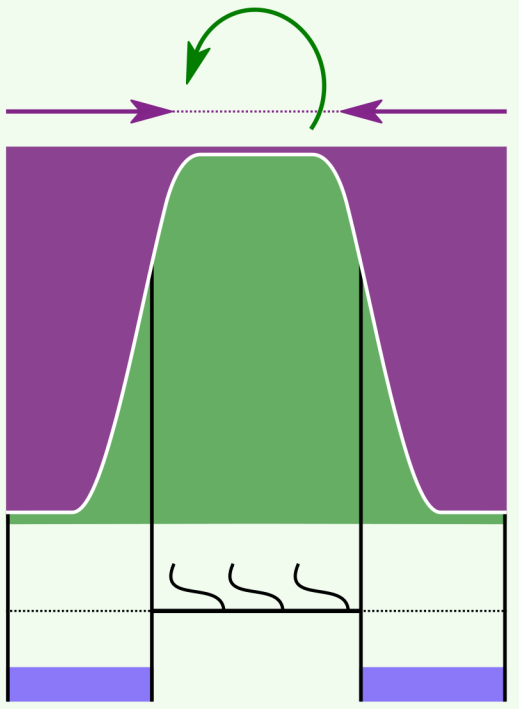

early initiation zones
(boundaries)

transcription + HIRA

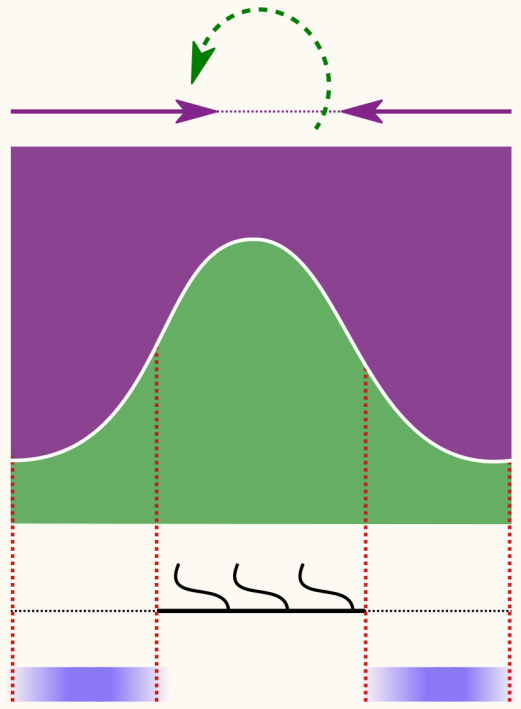

fuzzy initiation
(blurred sites)

deposition

occupancy

H3.1

H3.3

transcription

HIRA

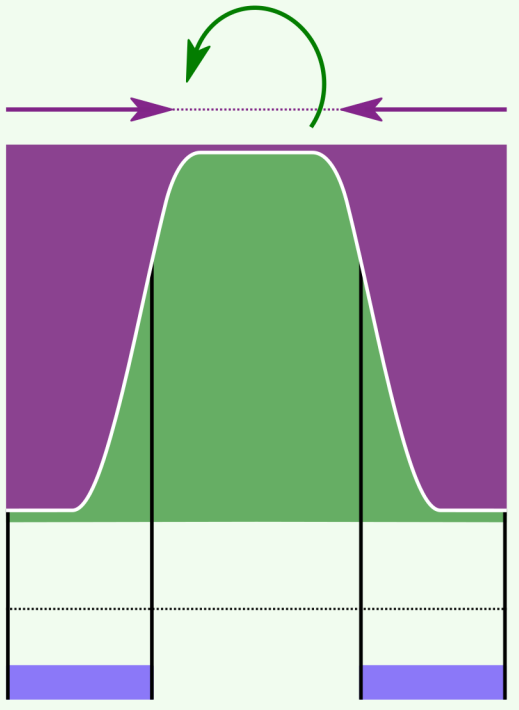

early initiation zones
(boundaries)

HIRA

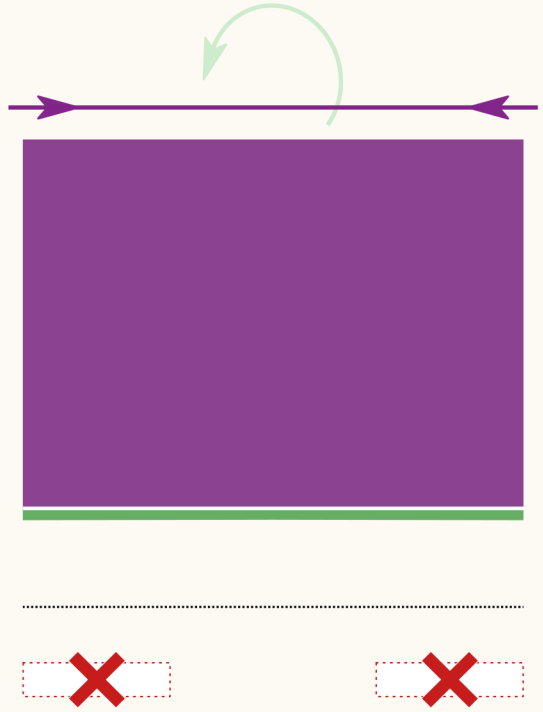

no early initiation
(buried sites)